THE ANALYZER OF SPACE PLASMAS AND ENERGETIC ATOMS (ASPERA-3) FOR THE MARS EXPRESS MISSION

S. BARABASH[1,*], R. LUNDIN[1], H. ANDERSSON[1], K. BRINKFELDT[1], A. GRIGORIEV[1], H. GUNELL[1], M. HOLMSTRÖM[1], M. YAMAUCHI[1], K. ASAMURA[2], P. BOCHSLER[3], P. WURZ[3], R. CERULLI-IRELLI[4], A. MURA[4], A. MILILLO[4], M. MAGGI[4], S. ORSINI[4], A. J. COATES[5], D. R. LINDER[5], D. O. KATARIA[5], C. C. CURTIS[6], K. C. HSIEH[6], B. R. SANDEL[6], R. A. FRAHM[7], J. R. SHARBER[7], J. D. WINNINGHAM[7], M. GRANDE[8], E. KALLIO[9], H. KOSKINEN[9,16], P. RIIHELÄ[9], W. SCHMIDT[9], T. SÄLES[9], J. U. KOZYRA[10], N. KRUPP[11], J. WOCH[11], S. LIVI[7], J. G. LUHMANN[12], S. McKENNA-LAWLOR[13], E. C. ROELOF[14], D. J. WILLIAMS[14], J.-A. SAUVAUD[15], A. FEDOROV[15] and J.-J. THOCAVEN[15]

[1]*Swedish Institute of Space Physics, Kiruna, Sweden*
[2]*Institute of Space and Austranautic Studies, Sagamichara, Japan*
[3]*University of Bern, Physikalisches Institut, Switzerland*
[4]*Instituto di Fisica dello Spazio Interplanetari, Rome, Italy*
[5]*Mullard Space Science Laboratory, University College London, Surrey, UK*
[6]*University of Arizona, Tucson, USA*
[7]*Southwest Research Institute, San Antonio, USA*
[8]*Rutherford Appleton Laboratory, Oxfordshire, UK*
[9]*Finnish Meteorological Institute, Helsinki, Finland*
[10]*Space Physics Research Laboratory, University of Michigan, Ann Arbor, USA*
[11]*Max-Planck-Institut für Sonnensystemforschung, Katlenburg-Lindau, Germany*
[12]*Space Science Laboratory/University of California in Berkeley, Berkley, USA*
[13]*Space Technology Ltd., National University of Ireland, Maynooth, Co. Kildare, Ireland*
[14]*Applied Physics Laboratory/John Hopkins University, Laurel, USA*
[15]*Centre d'Etude Spatiale des Rayonnements, Toulouse, France*
[16]*University of Helsinki, Helsinki, Finland*
*(*Author for correspondence: E-mail: stas@irf.se)*

(Received 23 August 2006; Accepted in final form 17 November 2006)

Abstract. The general scientific objective of the ASPERA-3 experiment is to study the solar wind – atmosphere interaction and to characterize the plasma and neutral gas environment within the space near Mars through the use of energetic neutral atom (ENA) imaging and measuring local ion and electron plasma. The ASPERA-3 instrument comprises four sensors: two ENA sensors, one electron spectrometer, and one ion spectrometer. The Neutral Particle Imager (NPI) provides measurements of the integral ENA flux (0.1–60 keV) with no mass and energy resolution, but high angular resolution. The measurement principle is based on registering products (secondary ions, sputtered neutrals, reflected neutrals) of the ENA interaction with a graphite-coated surface. The Neutral Particle Detector (NPD) provides measurements of the ENA flux, resolving velocity (the hydrogen energy range is 0.1–10 keV) and mass (H and O) with a coarse angular resolution. The measurement principle is based on the surface reflection technique. The Electron Spectrometer (ELS) is a standard top-hat electrostatic analyzer in a very compact design which covers the energy range 0.01–20 keV. These three sensors are located on a scanning platform which provides scanning through 180° of rotation. The instrument also contains an ion mass analyzer (IMA). Mechanically IMA is a separate unit connected by a cable to

Space Science Reviews (2006) 126: 113–164
DOI: 10.1007/s11214-006-9124-8

the ASPERA-3 main unit. IMA provides ion measurements in the energy range 0.01–36 keV/charge for the main ion components H^+, He^{++}, He^+, O^+, and the group of molecular ions 20–80 amu/q. ASPERA-3 also was its own DC/DC converters and digital processing unit (DPU).

Keywords: space instrumentation, Mars solar wind – interaction

1. Introduction

The purpose of the Analyzer of Space Plasma and Energetic Atoms (ASPERA-3) experiment on-board the European Space Agency Mars Express mission is to investigate the solar wind – Mars interaction through the use of ion, electron, and energetic neutral atom (ENA) measurements. The Mars Express mission was designed to fulfill the requirement of remotely sensing the planet and thus is not ideally suitable for space plasma investigations. The main drawback is the absence of a magnetometer onboard the spacecraft. Therefore, the ASPERA-3 investigation focused its objectives in relation to planetological issues rather than plasma processes. The main focus of the ASPERA-3 investigation was given to studies of the solar wind – Mars interaction impact on the atmosphere and atmospheric evolution. In the introduction we describe how near-Mars space is coupled to the atmosphere, then review the ENA environment of the planet and explain how ENAs can be used to diagnose plasma – gas interactions. In the following sections we review the instrument, its individual sensors, subsystems, accommodation on the spacecraft, and briefly describe the science operation concept.

1.1. Impact of the Solar Wind – Mars Interaction on the Atmosphere

Because of Mars lacks an intrinsic magnetic field, the following basic features characterize the near-planet environment:

(1) the upper atmosphere/ionosphere is a subject of solar wind induced escape in the form of pick-up ions and bulk plasma escape;
(2) the solar wind deposits matter, momentum, and energy into the Martian upper atmosphere;
(3) the atmosphere is a subject of sputtering which is caused by planetary ions either extracted from the ionosphere or resulted from the exospheric neutrals ionization, picked-up by the solar wind, and accelerated back to the atmosphere;
(4) the main domains and boundaries are the collisionless bow shock, the magnetospheath, a boundary which excludes the solar wind (induced magnetosphere boundary or magnetic pile-up boundary), the photoelectron boundary separating the region dominated by the ionospheric photoelectrons;
(5) the local crustal magnetizations affect the solar wind interaction pattern.

Without the magnetic cavity of a magnetosphere to shield the upper atmosphere from the on-coming solar wind, Mars is a subject to comet-like atmosphere erosion processes and solar-wind-induced current systems. The solar wind induced atmospheric escape occurs through three main channels; ion pick – up, bulk thermal plasma removal, and sputtering. While the first channel is extensively investigated both theoretically and experimentally, the two other remain poorly constrained because up to now the relevant plasma investigations have not been conducted. However, bulk plasma escape and sputtering are most efficient at removing heavy molecules such as CO_2. The atmospheric carbon dioxide is critical for understanding the water evolution on Mars. It is the thick CO_2 atmosphere thought to be present 3–4 billions years ago that provided the strong green house effect needed to rise the atmosphere temperature to the level at which water could exist in the liquid form. Apart from the solar wind induced escape mechanics, in operation at Mars now are the Jeans escape process (affect mainly hydrogen and deuterium) and non-thermal photochemical escape processes. The relative contribution of all these processes to the overall atmospheric evolution is still unclear because all estimations are based mainly on models, which, because of complex feedbacks are still quite limited. Figure 1 based on the review by Lammer *et al.* (2003) provides a summary of the escape mechanisms at Mars and illustrates their relative importance. Actual measurements by the PHOBOS-2 spacecraft determined that the scavenging of planetary ions amounts to $(0.5–3) \times 10^{25}$ ions/s (Lundin *et al.*, 1991; Verigin *et al.*, 1991). The initial results from the Mars Express mission confirm the existence of the effective particle loss induced by the solar wind interaction and even show that the solar wind may reach much lower altitudes (ca. 330 km) than was previously thought (Lundin *et al.*, 2004). It was also established that the escaping flux consists approximately of an equal amount of O_2^+ and O^+ and some admixture of CO_2^+ (ca. 20%) (Carlsson *et al.*, 2006). The newly reported escape rates measured by ASPERA-3 (Barabash *et al.*, 2007) are a factor of 100 lower than the PHOBOS-2 numbers, a puzzling finding still to be explained.

The role of the Martian crustal magnetic anomalies (Acuña *et al.*, 1998) in the overall ion escape is still unclear and the effect on the thermosphere is still to be investigated in detail. As was shown by the Mars Global Surveyor (MGS) mission (Crider *et al.*, 2002) the magnetic anomalies do affect the global pattern of the solar wind interaction by "lifting" the magnetic pile-up boundary and screening the ionosphere from the access of magnetospheath electrons. The analysis of the MGS MAG/ER (Magnetometer and Electron Reflectrometer) data indicated that the precipitating solar wind particles can heat the Martian thermosphere and that the crustal magnetic fields can control the sites where precipitations occur (Krymskii *et al.*, 2003). However, the recent Mars Express results indicate that there are no well-pronounced effects on ion fluxes (Nilsson *et al.*, this issue) (interpretation of the Mars Express particle data is complicated by the absence of magnetic field measurements). Nevertheless, Mars Express observed a short burst of CO Cameron band emissions (strongest lines) interpreted as Martian aurora (Bertaux *et al.*, 2005)

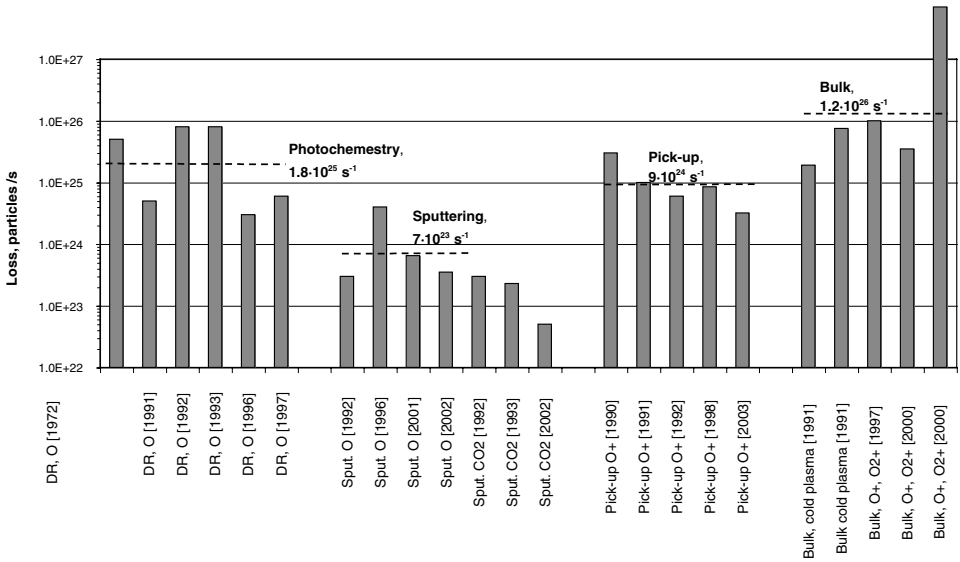

Figure 1. Non-thermal escape processes at Mars (adopted from review by Lammer *et al.*, 2003). DR: dissociative recombination; Sput.: sputtering. The horizontal dashed lines show log-averaged values. All available data, i.e., measurements, models, and estimations, are shown.

in the vicinity of a strong magnetic anomaly, indicating particle precipitation in the area. In addition, Lundin *et al.* (2006) reported signatures in Martian electron spectra above magnetic anomalies which are typical of those observed in terrestrial auroral electron spectra. The bulk escape might be the strongest among ion loss mechanisms driven by solar wind interactions (Figure 1). Ionospheric profiles observed by the Viking 1 and 2 landers indicate that the solar wind may erode the Martian ionosphere (Fox, 1997). Ionospheric bubbles or clouds triggered by plasma instabilities at the solar wind-ionopause transition region were observed on Venus and may also contribute to the loss of heavy ions as an additional escape process from the Martian ionosphere as shown in hybrid code simulations (Terada *et al.*, 2002). However, very limited experimental data are available to constrain the associated escape. Nairn *et al.* (1991) reported "tail rays," cold electron enhancements in the Martian tail with densities 10–65 cm^{-3} observed in association with broadband wave activity from a few Hz to several kHz. The associated ion outflow was estimated to $1.9–7.5 \times 10^{25}$ ions/s.

The atmospheric loss due to sputtering is the mechanism experimentally constrained the least, but is the key mechanism for determining the carbon dioxide inventory in the last Noachian Martian atmosphere because sputtering is the most effective way to remove CO_2. In light of the non-detection of carbonates on the surface (Bibring *et al.*, 2005), the current sputtering rate becomes the most important parameter which is used to constrain the amount of the carbon dioxide in the ancient Martian atmosphere.

Another problem of the solar wind – atmosphere coupling that has not been experimentally explored concerns the energetic consequences for the Martian atmosphere of the lack of a Martian dipole field. The kinetic and test-particle models of the Mars-solar wind interaction (Brecht, 1997; Kallio *et al.*, 1997) have suggested that solar wind absorption by the Martian atmosphere may be an important energy source for the upper atmosphere. The ENAs generated as a product of the solar – wind interaction further enhance the deposition of solar wind energy (Kallio and Barabash, 2000). According to the models, some of the solar wind ions (mainly protons and alphas) directly impact Mars' upper atmosphere near its exobase (at ~180 km altitude) because their gyroradii are too large to behave as a deflected "fluid" in the subsolar magnetosheath (Kallio and Janhunen, 2001) or because they are partially thermalized by the bow shock (Kallio *et al.*, 1997). Thus, solar wind energy is "directly" deposited into the upper atmosphere resulting in increasing ionization rates and UV emissions.

1.2. ENA Production and ENA Diagnostics

As a result of the low gravity on Mars, the neutral gas (exosphere) density can reach 10^4–10^6 cm^{-3} in the solar wind interaction region where the main plasma boundaries, the bow shock and the magnetic pile-up boundary (induced magnetosphere boundary), are located. The co-existence of these two components, the solar wind plasma and the planetary neutral gas, results in strong interactions. One of the fundamental collisional interactions is the charge – exchange process

$$A^+(\text{energetic}) + M(\text{cold}) \Rightarrow A(\text{energetic}) + M^+(\text{cold}),$$

that provides ENAs. A global image formed from the directional detection of ENAs yields a picture of this interaction region while analysis of the time variation of the ENA signal and of the ENA energy spectrum provides a means to diagnose the plasma properties exhibited within the interaction region. The main populations of ENAs at Mars are described in Table I and the hydrogen ENA flux morphology is depicted in Figure 2.

The supersonic solar wind upstream of the bow shock can experience charge – exchange with the Martian hydrogen exosphere over very long distances resulting in a narrow ($\cdot\cdot 10^\circ$) anti-sunward beam of ENAs called the neutral solar wind which has an energy of the bulk flow of the solar wind. This population was detected by the Low Energy Neutral Atom (LENA) instrument onboard the terrestrial magnetospheric Imager for Magnetopause-to-Aurora Global Exploration (IMAGE) mission (Collier *et al.*, 2001) which was capable of looking directly towards the Sun. This component can also be measured with sensors not fully immune against solar UV photons from vantage points inside the Martian eclipse (Brinkfeld *et al.*, 2006). In this geometry,

TABLE I
ENA at Mars.

Original ion/neutral population	Production mechanism	ENA Energy
Upstream solar wind (Holmström *et al*., 2002)	Charge – exchange of the undisturbed solar wind on the extended hydrogen exosphere	∼1 keV
Shocked solar wind (Holmström *et al*., 2002; Gunell *et al*., 2006)	Charge – exchange of the shocked solar wind on the hydrogen corona in the magnetospheath	Few hundreds eV
Accelerated planetary ions (Barabash *et al*., 2002; Lichtenegger *et al*., 2002)	Charge – exchange of H^+, O^+, O_2^+, CO_2^+ on the neutral coronae (H, H_2, O)	Few hundreds eV – few keV
Backscattered hydrogen (ENA albedo) (Kallio and Barabash, 2001; Holmström *et al*., 2002)	Backscattering of the precipitating neutral solar wind and solar wind protons from the upper atmosphere	Few hundreds eV
Sputtered O and CO_2 (Luhmann and Kozyra, 1991; Luhmann *et al*., 1992)	Sputtered of the atmospheric gasses by precipitating O^+	Few tens eV (low flux)
Phobos torus (Mura *et al*., 2002)	Charge – exchange of the solar wind (upstream/shocked) on the neutral gas density increase due to possible Phobos torus.	Few hundreds eV

Mars blocks the solar photons but neutral solar wind can reach the umbra region due to thermal spreading and scattering by the upper atmosphere (Kallio *et al.,* 2006).

The shocked solar wind is the strongest source producing ENAs since the protons flowing around the Martian obstacle have the most time to interact with the dense (in the ENA context) hydrogen exosphere. Detailed modeling of the ENA production from this source was performed by Kallio *et al*. (1997), Holmström *et al*. (2002), Mura *et al*. (2002), and Gunell *et al*. (2006). Figure 3 taken from Gunell *et al*. (2006), shows simulated ENA images for several vantage points at different solar zenith angles. The estimated ENA fluxes are well above $10^4\,cm^{-2}\,s^{-1}\,keV^{-1}$ and the directional fluxes exceed $10^5\,cm^{-2}\,s^{-1}\,sr^{-1}$ (images for solar zenith angle 80°, 100°, and 120°).

Barabash *et al*. (2002) and Lichtenegger *et al*. (2002) investigated the detailes of the ENA signal associated with oxygen and hydrogen pick-up ions. Using the empirical model of the solar wind plasma flow near Mars developed by Kallio

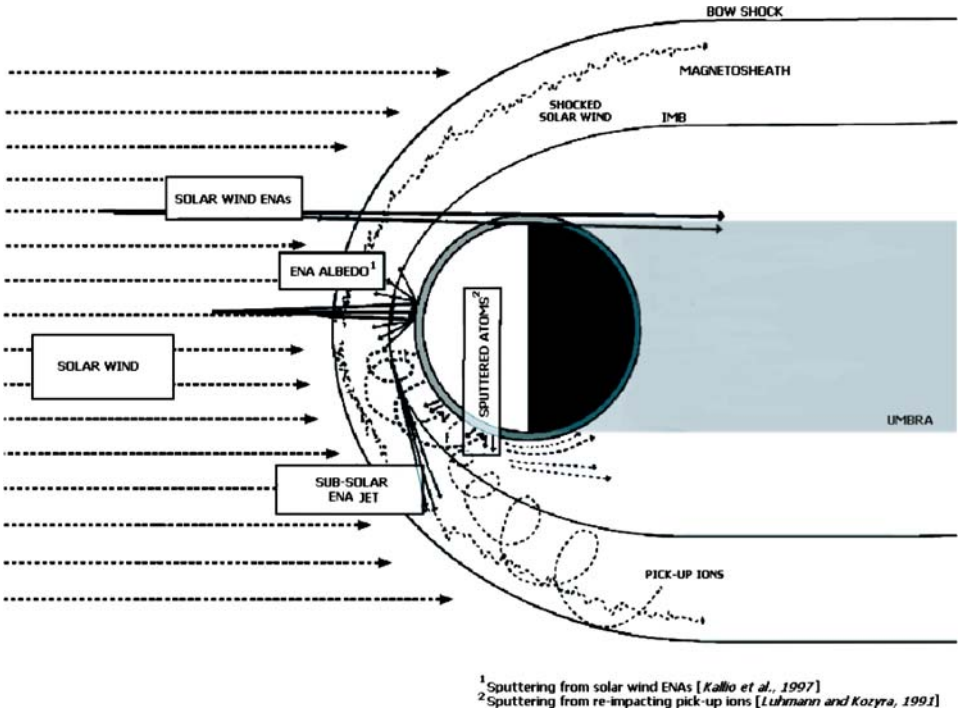

Figure 2. ENA populations at Mars. Not shown are ENAs which originated from the planetary ion charge – exchange (From Brinkfeld *et al*., 2006).

(1996), Barabash *et al*. (2002) numerically solved the kinetic equation to obtain the global distribution of oxygen ions. This distribution was then converted to the corresponding ENA flux. It was found that the fluxes of oxygen ENAs could reach 10^4 cm^{-2} s^{-1} sr^{-1} eV^{-1} and fully reflect the morphology of the oxygen population. This process provides a technique for determining the instantaneous oxygen escape rate. One of the simulated images for the energy range 0.1–1.65 keV is reproduced in Figure 4. The projection is similar to the one used to display the hydrogen ENA images of Figure 3. The Figure 4 image shows a strong jet of ENAs coming out from the subsolar point and flowing tailward.

ENA images reveal morphological features of the ENA sources such as locations of boundaries and relative sizes. Directionally separated ENA signals can be converted into global distributions of the proton flow and of neutral gas using inversion techniques similar to those developed for conditions at the Earth (Roelof and Scinner, 2000). Holmström *et al*. (2002) showed that the ENA fluxes generated from the shocked solar wind are the most sensitive to the neutral hydrogen distribution, which is controlled by the exobase temperature, and the position of the boundary separating the solar wind and planetary plasmas.

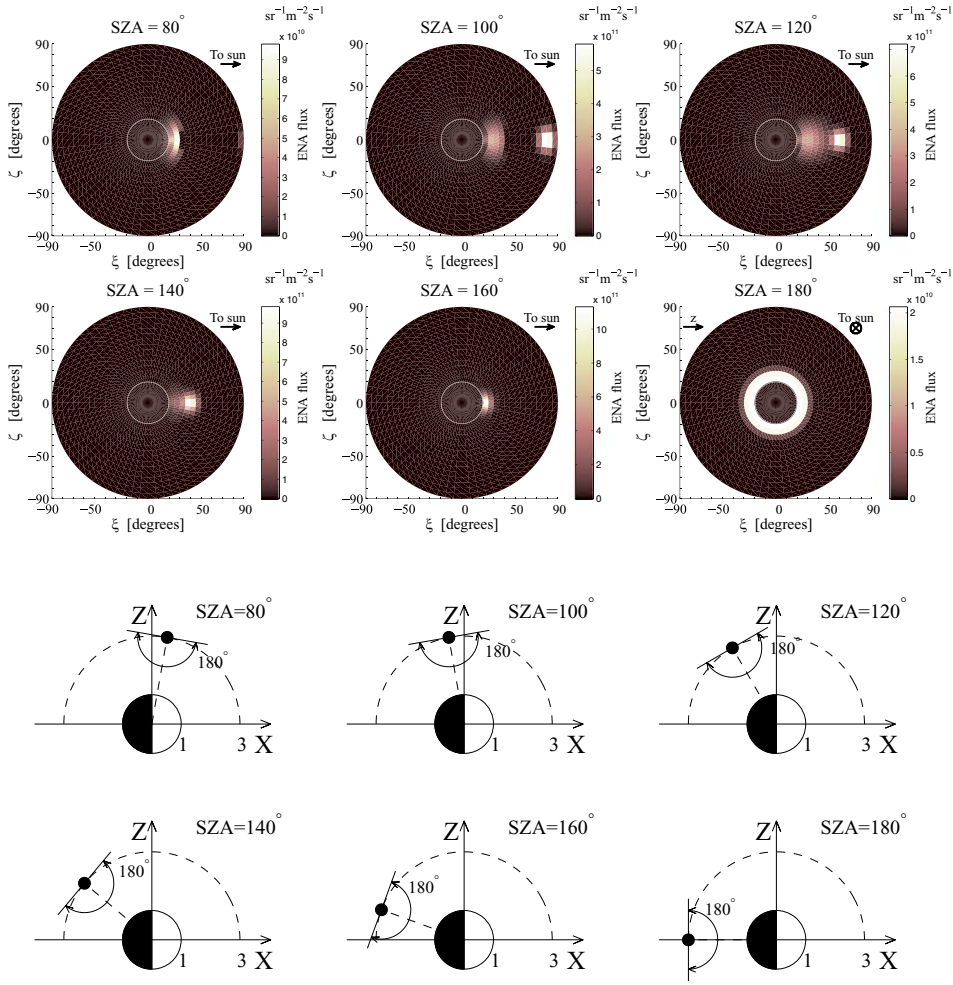

Figure 3. Hydrogen ENA images. The ENA images are from vantage points which are 3Rm from the center of Mars looking towards nadir. The solar zenith angles (SZA) are from 80° to 180°. The horizontal and vertical axes show the angular offsets in degrees, from the centre of the image (from Gunell *et al*., 2006).

The directionally separated ENA signals of the escaping plasma display globally and instantaneously the size and geometry of the outflowing plasma as well as provide constrains on the total escape rate (Barabash *et al*., 2002). For example, the non-detection of oxygen ENAs by the ASPERA-3 sensor has constrained the total escape rate of oxygen to be "less than 1 g/s" (Galli *et al*., this issue), which is close to the 4 g/s obtained by direct measurements using the ion plasma spectrometer (Barabash *et al*., 2006).

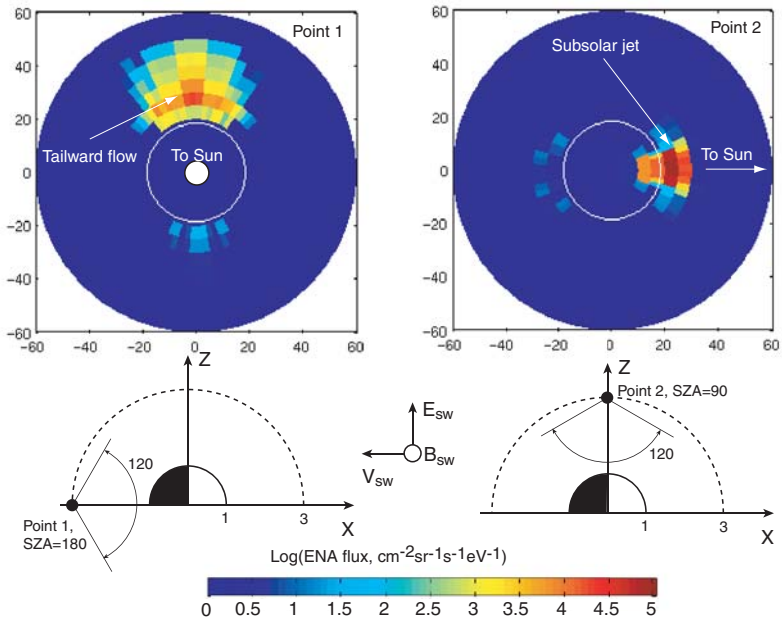

Figure 4. ENA images of pick-up oxygen ions from two vantage points: in the tail and at the pole. The vantage points are in the plane perpendicular to the ecliptic. The polar axis is towards the planetary center. The image projection is similar to those shown in Figure 3. The energy range is 0.1–1.65 keV. The electric and magnetic field vectors in the solar wind are also shown for reference (Adopted from Barabash *et al.*, 2002).

ENA diagnostics is a useful tool in the study of plasma dynamics because temporal and spatial variations are inherently separated. A single directional observation provides measurements of the typical time scale for plasma variations in the interaction region. The global response of the system against internal disturbances can also be studied, for example, variations of the magnetic pile-up boundary during interplanetary shock impact or internal variability related to different kinds of instabilities (Futaana *et al.*, this issue; Grigoriev *et al.*, this issue). Imaging ENA albedo, i.e., ENAs resulted from back scattering and sputtering, can be used to map the precipitation fluxes.

2. Scientific Objectives

In order to study the processes related to the atmospheric impact of the solar wind – Mars interaction on the atmosphere, the ASPERA-3 experiment was designed to measure electrons and ions in the hot plasma energy range as well as to provide remote sensing (diagnostics) of the plasma – neutral gas interaction *via* ENA measurements. The key objectives of the ASPERA-3 experiment are (1) to determine

TABLE II
The ASPERA-3 objectives and requirements.

Scientific objectives	Measurements requirements
Solar wind induced ion escape (pick-up, bulk escape, sputtering)	Mass resolving ion measurements in the energy range few eV – tens keV
	Mass resolving (H/O) ENA measurements in the energy range few eV – tens keV. ENA flux $>10^3$ cm^{-2} s^{-1} keV^{-1}
Momentum, energy, and mass deposition from the solar wind to the upper atmosphere/ionosphere	Mass resolving ion and electron measurements in the energy range few eV – tens keV
	Mass resolving (H/O) ENA measurements in the energy range down to tens eV from the nadir direction. ENA flux $>10^6$ cm^{-2} s^{-1} keV^{-1} (100 eV)
Morphological structure of the Martian interaction region and local plasma characteristics	Mass resolving ion and electron measurements in the energy range few eV – tens keV with 4π coverage
	Measurements of the ENA flux in the energy range tens eV – few keV with 4π coverage.
	ENA flux $>10^4$ cm^{-2} s^{-1} keV^{-1}
	Measurements of the upstream solar wind parameters.
Search for the solar wind – Phobos interactions	Mass resolving ion and electron measurements in the energy range few eV – tens keV
	ENA measurements in the energy range tens eV – few keV with 4π coverage. ENA flux 10^4 cm^{-2} s^{-1} keV^{-1}

as precisely as possible the total ion escape (particles/s) for the major ion species (O, O_2^+, CO_2^+), (2) to study momentum, energy, and mass deposition from the solar wind into the upper atmosphere/ionosphere and its response (sputtering), (3) to investigate the morphological structure of the Martian interaction region and define its local plasma characteristics. A search for the solar wind – Phobos interaction was also undertaken. The ASPERA-3 objectives and associated measurement requirements are listed in Table II.

The scientific objectives of ASPERA-3 are formulated to describe the current solar wind interaction with Mars. The results of the experiment can be projected backward in time in order to determine the reaction of the planet at times past. Thus, results of the ASPERA-3 investigation are instrumental in determining and

constraining the role of the solar wind interaction in the overall atmosphere evolution throughout the history of Mars.

3. The Instrument

No instruments with similar scientific objectives and capabilities of ASPERA-3 have been or are planned to be flown to Mars. The only similar experiment, ASPERA-C, was on-board the Mars-96 mission; however, the ASPERA-C did not contain a mass-resolved energy-analyzing ENA detector. The Japanese Nozomi spacecraft, launched to Mars in 1998, was concentrating on plasma measurements, but it did not carry any ENA detectors. Both the Mars-96 and Nozomi missions failed to reach Mars. MGS (launched in 1996 operational until November 2006) carried a magnetometer and an electron spectrometer (energy resolution 25%), but contained no ENA or ion measurement capability.

3.1. Overview

Mechanically the ASPERA-3 instrument consists of two units, the Main Unit (MU) and the Ion Mass Analyzer (IMA) (Figure 5). The MU comprises three sensors Neutral Particle Imager – NPI, Neutral particle Detector – NPD, Electron Spectrometer – ELS and a Digital Processing Unit – DPU, which are all located on a scanner. The MU is also equipped with two solar sensors allowing identification of the Sun direction for automatic reduction of the detector bias during scanning because the ENA sensors are UV sensitive. All mechanical and electrical interfaces are made through the scanner. The total mass of the instrument is 8.2 kg and the power consumption is ca. 16 W. The MU envelope is $359 \times 393 \times 234\,\mathrm{mm}^3$ and the IMA envelope is $255 \times 150 \times 150\,\mathrm{mm}^3$.

NPI provides measurements of the integral ENA flux with no mass or energy resolution but with $5^\circ \times 11^\circ$ angular resolution. The intrinsic field of view is $9^\circ \times 344^\circ$. The sensor utilizes the particle – surface interaction technique for ENA detection. ENAs incident on a target surface coated by a graphite – containing material (DAG 213, a resin-based graphite dispersion) at a grazing angle of 20° are reflected and/or cause ion sputtering. An MCP (Microchannel Plates) stack detects the reflected particles and sputtered fragments with a discrete anode. The NPI head is a replica of the NPI-MCP sensor developed for the ASPERA – C experiment on the Mars-96 mission (launch failure) and successfully flown on the Swedish microsatellite Astrid launched in 1995 (C:son Brandt *et al.*, 2000). A detailed overview of the NPI development and calibration results including UV response can be found in Brinkfeldt (2005). The NPI also accommodates two solar sensors.

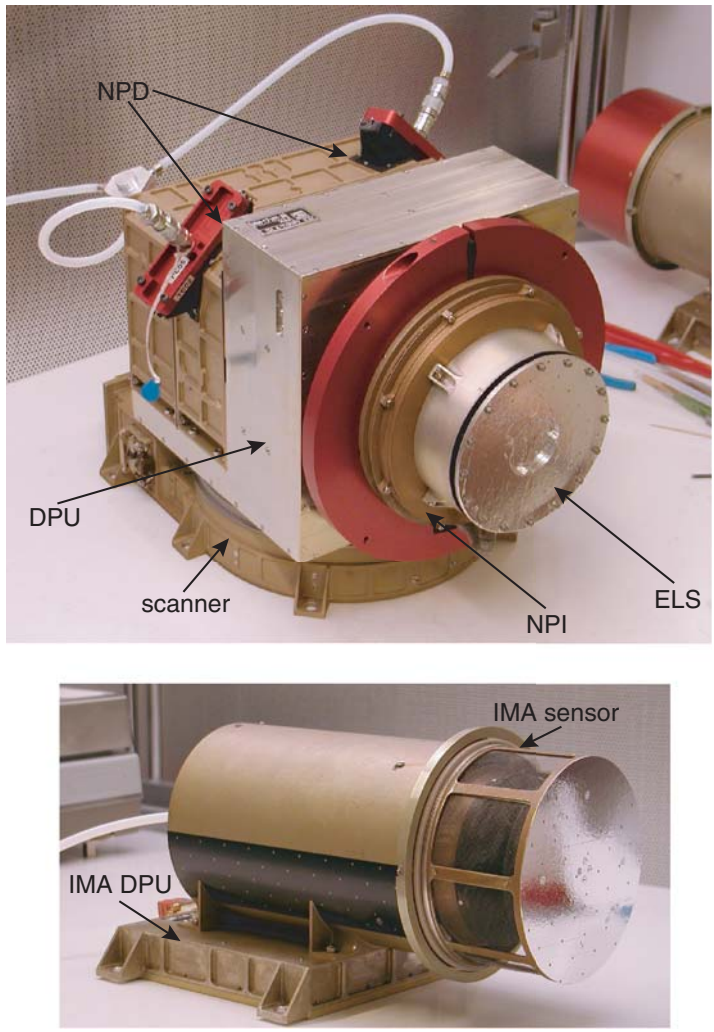

Figure 5. The ASPERA-3 configuration (flight model with red-tagged covers installed).

The NPD provides measurements of the ENA differential flux over the energy range 100 eV–10 keV, resolving H and O with coarse ($5^\circ \times 30^\circ$) angular resolution. The sensor consists of two identical heads, each with the $9^\circ \times 90^\circ$ intrinsic field of view. The measurement technique is based on the principle similar to NPI. ENAs incident on a surface at a grazing angle of 15° are reflected and cause secondary electron emission. The secondary electrons are transported to an MCP assembly, which gives the START signal. The reflected ENAs hit a second surface and again produce secondary electrons used to generate the STOP signal. The NPD time-of-flight (TOF) electronics determines the ENA velocity. Mass analysis is based on the

large velocity difference between two main ENA species, hydrogen and oxygen. The pulse – height distribution (PHD) analysis of the STOP signals can also be used to provide a rough determination of the ENA mass.

ELS provides electron measurements in the energy range 0.01–20 keV. The intrinsic full field of view is $4^\circ \times 360^\circ$. The 360° aperture is divided into 16 sectors. The sensor is a standard top – hat electrostatic analyzer in a very compact design. ELS is a reduced and modified version of the Miniaturized Electrostatic Dual-top-hat Spherical Analyzer (MEDUSA) experiment for the Astrid-2 and Munin missions launched in 1998 and 2000 (Norberg *et al.*, 2001).

IMA is an improved version of the Three-dimensional Ion Composition Spectrometer (TICS)/Freja, Ion Mass Imaging Sensor (IMIS)/Mars-96, Ion Mass Imager (IMI)/Nozomi (Norberg *et al.*, 1998), and an exact copy of the Ion Composition Analyzer (ICA) instrument flying on the Rosetta mission. In the ASPERA-3 design, the IMA is a separate unit connected by a cable to the MU. The IMA provides ion measurements in the energy range 0.01–36 keV/q for the main ion components H^+, H_2^+, He^+, O^+, and for the group of molecular ions $20 < M/q < \sim 80$. The IMA instantaneous field of view is $4.6^\circ \times 360^\circ$. Electrostatic sweeping performs elevation ($\pm 45^\circ$) coverage. The IMA sensor is a spherical electrostatic analyzer followed by a circular magnetic velocity separating section. A large diameter MCP with a discrete anode system images a matrix, which is azimuth $\times$ mass.

The three sensors (NPI, NPD, and ELS) are located on a scanning platform. The combination of the 360° field of view of NPI and ELS along with the scanner motion from 0° to 180° could provide the 4π maximum coverage; however, a fraction of the field of view is blocked by the spacecraft body. The scanner also provides the capability of pointing ELS, NPI, and NPD independently of the spacecraft. Table III summarizes the instrument performance.

The following features make ASPERA-3 a truly unique instrument:

(1) two ENA sensors, the first at Mars
(2) combined electron, ion, and ENA sensors in a single package with common data acquisition system
(3) high energy resolution of electron measurements (8%) ensuring resolving photoelectron peaks.

Mars Express has quite a favorable orbit for studies of the solar wind – planet interaction. With its pericenter height of 270 km and apocenter of 11,580 km (first year in-orbit) and 10,050 km (later in the mission), the 86.6° inclination the orbit allows sampling of all plasma domains, and during certain periods, grazes the induced magnetosphere boundary (magnetic pile-up region) for hours.

TABLE III
Performance of the NPI, NPD, ELS, and IMA sensors.

Parameter	NPI	NPD	ELS	IMA
Particles to be measured	ENA	ENA	Electrons	Ions
Energy range, keV per charge	≈0.1–60[a]	0.1–10	0.01–20	0.01–30
Energy resolution, $\Delta E/E$	No	0.5	0.08	0.07
Resolved masses, amu/q	No	1, 16	N/A	1, 2, 4, 8, (16, 32, 44)[b]
Intrinsic field of view	$9^\circ \times 344^\circ$	$9^\circ \times 180^\circ$	$4^\circ \times 360^\circ$	$90^\circ \times 360^\circ$
Angular resolution (FWHM)	$4.6^\circ \times 11.5^\circ$	$5^\circ \times 40^\circ$	$2^\circ \times 22.5^\circ$	$4.5^\circ \times 22.5^\circ$
G-factor/pixel or sector cm^2 sr (NPI, NPD) cm^2 sr eV/eV (ELS, IMA)	2.5×10^{-3} (ε not incl.)	6.2×10^{-3} (ε not incl.)	7×10^{-5}	1.6×10^{-6}
Efficiency, ε, %	∼1	1–15	Inc. in G	Inc. in G
Time resolution (one scan), s	32	32	32	196[c]
Mass, kg	0.7	1.3	0.3	2.2
Power, W	0.8	1.5	0.6	3.5

[a]Upper cut-off of the deflector system.
[b]The ions O^+, O_2^+, CO_2^+ (mass/charge = 16, 32, 44) are resolved by peak-fitting technique (Carlsson *et al.*, 2006).
[c]Full energy – elevation scan.

3.2. Neutral Particle Imager (NPI)

The significant components of NPI are identified in Figures 6–8. Figure 6 identifies the main components of NPI in a cross-sectional view while the integrated sensor is shown in Figure 7 . At selected locations during assembly, the critical components of NPI are identified in Figure 8 (the actual NPI shown here is from ASPERA-4 for the Venus Express mission, identical to the ASPERA-3 NPI except for the outer structure surface thermal coating). The charged particles, electrons and ions, are removed by the electrostatic deflection system, which consists of two disks separated by a 3 mm gap. The 5 kV positive potential between the grounded and biased disks results in a strong electric field, which sweeps away all charged particles with energies up to 60 keV. Since the integral ENA flux substantially exceeds the

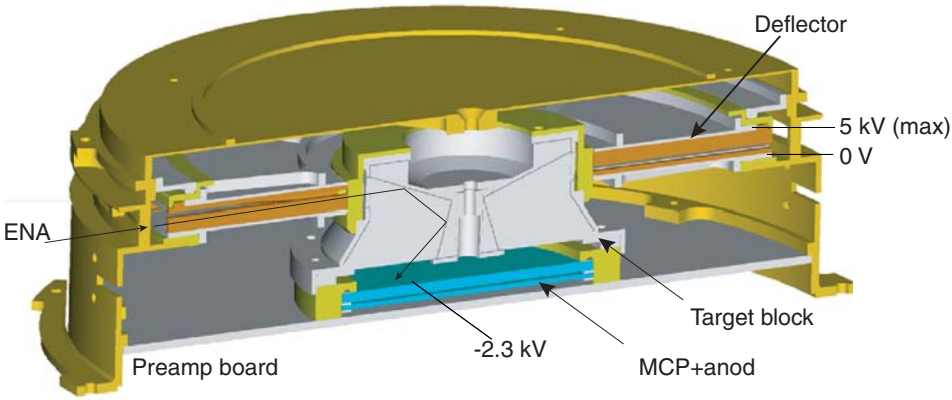

Figure 6. NPI sensor cross-sectional view. The deflector voltage and MCP bias are identified.

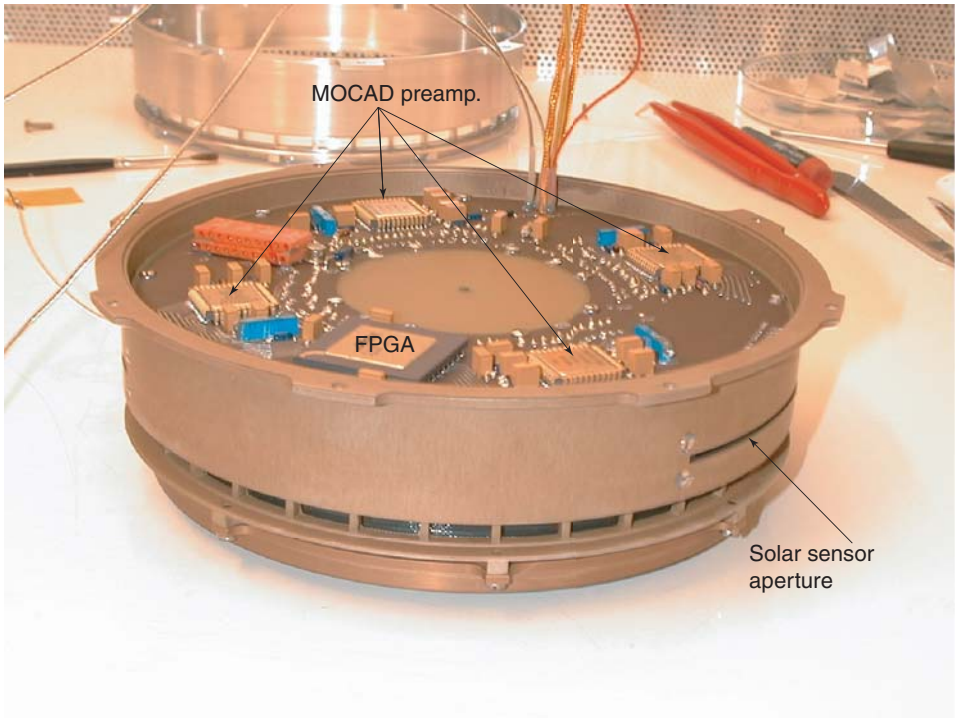

Figure 7. The completed NPI sensor.

charged particle flux for energies greater than 60 keV, this rejection energy is sufficient for satisfactory performance. The disks also collimate the incoming beam over elevation and azimuth angle. Apart from being ON or OFF, the deflection system can be operated in two other modes, alternative mode and sweeping mode.

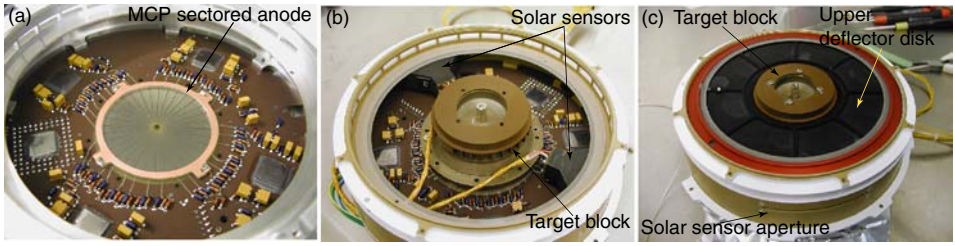

Figure 8. NPI components: the sectored anode (a), the target block installed (b) and the deflection system installed (c).

In the alternative mode, the deflection system is turned on and off, alternating each sampling period; whereas, in sweeping mode, the potential across the deflection system is continually changed to form a voltage sweep. These modes are used to more accurately separate charged and neutral particles entering the system. The deflection system is connected to the high voltage supply *via* an optocoupler. Regulating the optocoupler reference voltage causes changes in the deflection voltage performing the sweeping and alternating. In order to reduce the time for discharging of the deflection system disks down to 1 ms, a second parallel optocoupler is used.

The space between the deflection system disks is divided into 32 sectors by plastic (PEEK) spokes which form 32 azimuthal collimators, each with a field of view of $9^\circ \times 18^\circ$ and an angular resolution of $4.6 \times 11.25^\circ$ (full width at half maximum, FWHM). Neutrals passing through the deflection system hit a 32 sided cone target at a grazing angle of incidence of 20°. The interaction of the neutrals with the target results in secondary particle production, both electrons and ions, and/or reflection of the primary neutrals. A 56 mm diameter PHOTONIS MCP stack in chevron configuration followed by a 32 sector anode detects the particles leaving the target. The signal from the MCP gives the direction of the primary incoming neutral. The MCP operates in ion mode with a negative bias of slightly more than -2.3 kV applied to the front side of the MCP stack, and thus, detects (a) sputtered positive ions of the target material, (b) positive ions resulting from ionizing of the primary neutrals, and (c) neutrals reflected from the target surface. In order to improve the angular resolution and collimate the particles leaving the interaction surface, 32 separating walls are attached to the target forming a star-like structure. This configuration allows the entering particles to experience multiple reflections and reach the MCP. NPI covers 4π in one half scanner cycle (except for the fraction blocked by the spacecraft body) and produces an image of the ENA flux distribution in the form of an azimuth $\times$ elevation matrix once per (32s, 64s, or 128s). The flux in each of the 32 elements is read out once every 62.5 ms and integrated over 1 s by the DPU. Two sectors around the scanner spin axis and looking toward the spacecraft body are blocked, intended to provide monitoring of the MCP assembly dark counts. This space is also used to connect the ELS electrical

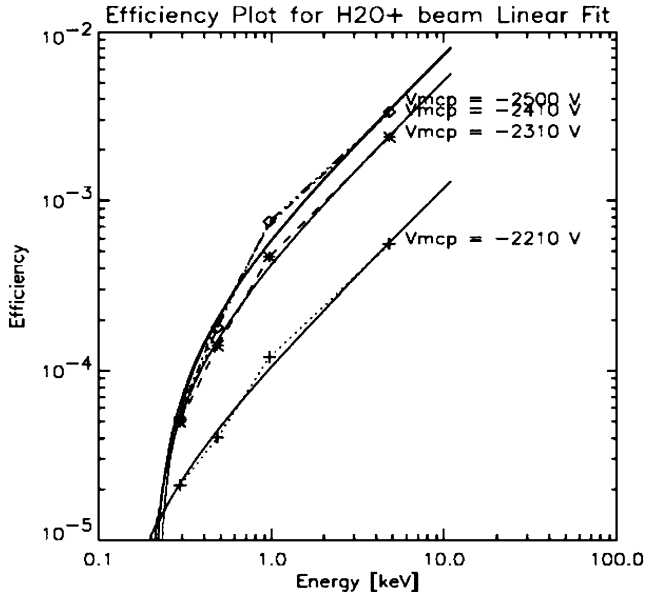

Figure 9. The NPI efficiency of the sector 14 with neighboring sectors mechanically blocked against H_2O beams for different bias voltages and energies.

harness to the DPU. The NPI sensor also accommodates two solar sensors which can be seen in Figures 7 and 8.

NPI calibrations were performed at the Swedish Institute of Space Physics, Kiruna, Sweden jointly with Institute of Space and Astronautic Studies, Sagamichara, Japan as well as at the University of Arizona, Tucson, United States of America. Calibrations of the NPI sensor were preformed to characterize the sensor response, MCP working bias, dark count level, angular response in elevation and azimuth, and efficiency. In addition, comprehensive investigations of the sensor's immunity against UV photons were performed.

The MCP working bias is a bias at which the MCP count rate starts to saturate for a given discriminator level. During calibrations, the measurement of the MCP count rate saturation started at slightly more than an MCP bias of -2.4 kV. However, to optimize the angular resolution, the MCP operational bias was chosen to be -2.3 kV (Brinkfeldt, 2005).

Figure 9 shows the NPI efficiency for different values of the MCP bias and for different particle energies using H_2O^+ beams. The efficiency was measured in sector 14 where the neighboring sectors were mechanically blocked. This single sector was thoroughly investigated in terms of efficiency measurements. The NPI sector 14 efficiency of the solar wind at an energy of 1 keV is around 5×10^{-4} for an operating bias of 2.3 kV. An azimuth scan of all sectors with the particle beam located in the central plane (shown in Figure 10) was used to determine the relative

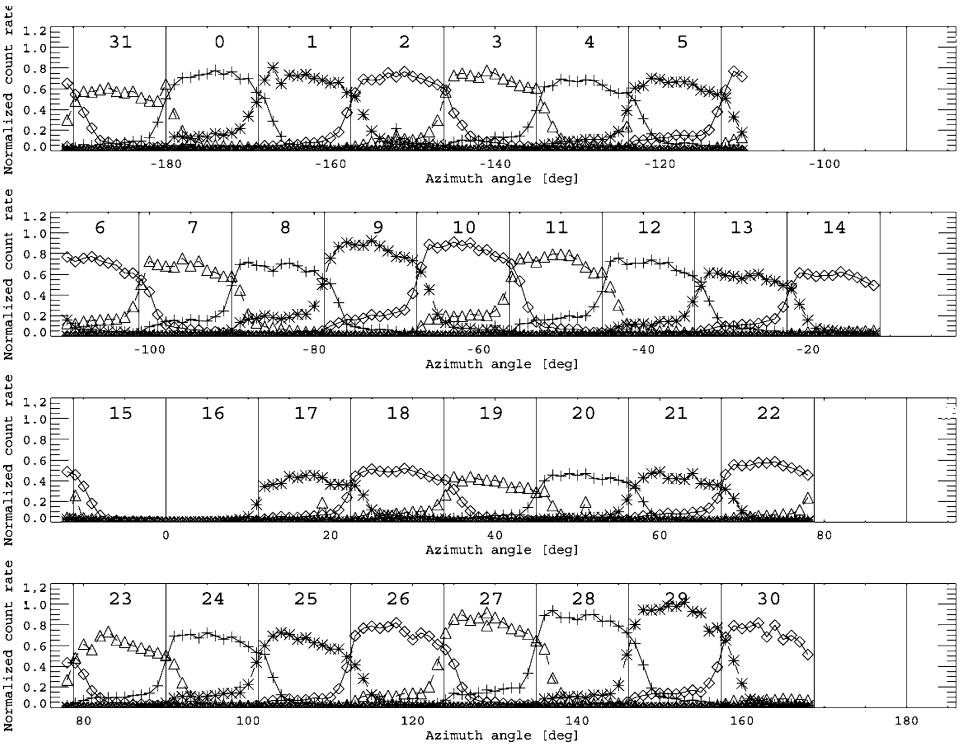

Figure 10. Scan through the central plane of the NPI sectors showing the relative efficiency against a H_2O^+ beam.

response of the other 31 sectors and define inter-calibration factors for each NPI sector. The azimuthal scan shows that there are large differences in the response of different sectors and the defined inter-calibration factors are significant. For example, sectors 17–21 show lower responses than the remaining sectors (sectors 15 and 16 are mechanically blocked and used to monitor MCP background). The sensitivity variation between different sectors is about a factor of 2 and the inter-calibration factors need to be taken into account during ENA image processing. At the nominal operation bias, Figure 11 shows the angular response of sector 14 to a 5 keV beam of protons. The lower plots in Figure 11 show a polynomial fit to the response. The analytical function describing the sensor angular response is included into ENA image inversion software performing ENA image inversion.

The calibration provided a pure geometrical factor of 2.7×10^{-3} cm^2 sr, not including the efficiency. This number is also confirmed by ray-tracing. The equation below can be used to convert from the count rate in sector n, C_n, to the flux F_n

$$F_n = \frac{C_n - C_{\text{dark}}}{G\eta_n\varepsilon}$$

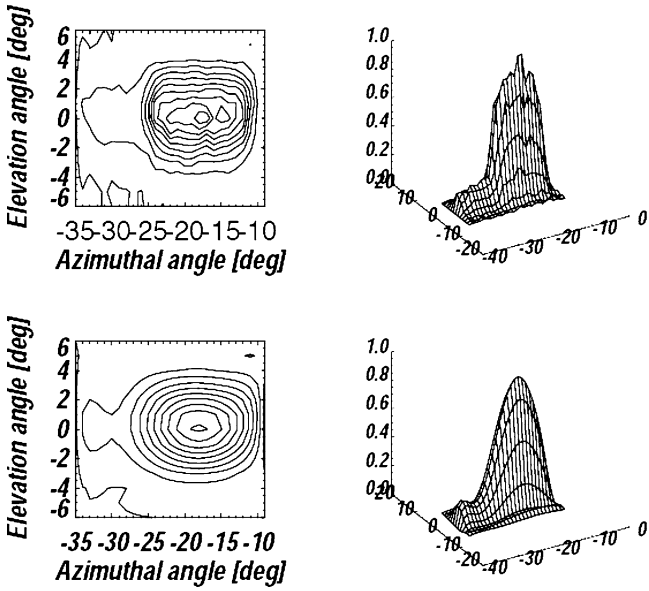

Figure 11. Full angular response of the sector 14 against a proton beam. The lower plot is a polynomial fit.

where C_{dark} is the dark count of sector n (defined during calibrations and monitored in flight through the count rate of the blocked sectors 15 and 16), G is the pure geometrical factor, η_n is the relative sensitivity to sector 14, and ε is the efficiency of sector 14.

An important issue in the NPI design is coating the target block for suppression of UV photon fluxes, which enter the instrument and produce a UV background in the measurements. NPI uses the same coating as in the Prelude in Planetary Particle Imaging (PIPPI) and NPI/ASPERA-C experiments, namely, DAG 213, a resin-based graphite dispersion. This substance is similar to Aquadag, which is a graphite dispersion in water. The coating demonstrated satisfactory performance in the PIPPI experiment flown in the Earth's magnetosphere (C:son Brandt *et al.*, 2000). To verify the expected UV contamination levels the Mars Express NPI spare model (the ASPERA-4 flight model) was calibrated against Lyman-α photons ($\lambda = 121.6$ nm). The calibration philosophy was similar to that of the particle calibration, i.e., the response of one sector (number 4) was fully characterized and then a relative measurement was made for the other sectors.

Using a much simpler set-up (Barabash, 1995), the previous measurement gave the DAG 213 UV rejection efficiency around 10^{-5}.The efficiency of the MCP itself for UV at the Lyman-α wavelength is $\sim$1%. So the combined efficiency of the NPI for Lyman-α photons was expected to be 10^{-7}.

Figure 12a shows the dependence of a single channel count rate (sector 4) on UV beam intensity. The count rate was determined by integrating over angle. The

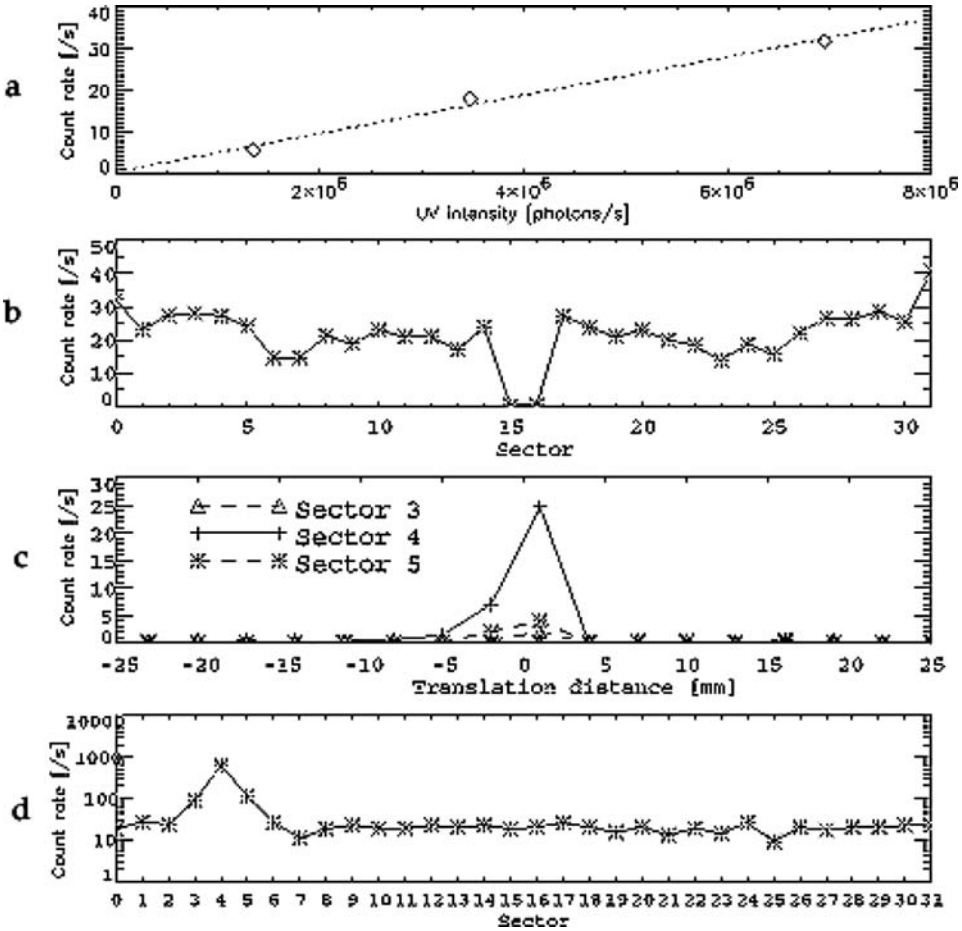

Figure 12. (a) Absolute UV calibration results. NPI count rate (sector 4) as a function of the Lyman – α photon flux. (b) Relative sensitivity of the NPI sectors against UV. (c) NPI sectors 3, 4, and 5 response during a translation perpendicular to the UV beam. (d) The count rate for each sector during the translation of the sensor perpendicular to the UV beam.

parallel UV photon beam was centered about sector 4. Due to limitations in the beam intensity variations, only three points on this curve were determined. The detection efficiency was found to be 5×10^{-6}, close to the previous (less accurate) measurements. The response of the other 31 sectors against Lyman- α photons was measured only at the center of the aperture of each sector, following the approach similar to the particle calibrations. The count rate normalized to the same beam intensity is shown in Figure 12b. Sectors 15 and 16 show zero counts because they are mechanically blocked. In general, the UV sensitivity varies by a factor of 2 between different sectors, similar to the particle measurements. This result indicates that there are gain variations across the MCP surface.

To investigate internal photon reflection from the deflector spokes separating the different sectors, the sensor performed parallel translation with respect to the UV beam, again with the center of the UV beam directed at the center of sector 4 when directly under the UV beam. Figure 12c shows responses from sector 4 (center parallel to the beam) and two neighboring sectors 3 and 5 (each centered 11.25° from parallel) resulting from the translation. Figure 12d shows the integrated count rate for each different sector during the translation. This test showed that internal photon reflections result in a cross-talk between neighboring sectors to a level of 10–15%.

The sensor includes only front-end-electronics (FEE) and interfaces with the DPU *via* an FPGA (Field Programmable Gate Array). High voltage is provided by an external high voltage supply located inside the DPU. The FEE is based on 4 MOCAD (Monolitic Octal Charge Amplifier/Pulse Discriminator) chips each containing 8 channels. The signals from the MCP anode are fed directly to the MOCAD inputs, which generate Transistor–Transistor Logic (TTL) pulses. The discriminator threshold is the same for all 8 channels. The sensitivity may vary between different channels within a chip which may also contribute to the variations in efficiency observed between sectors (Figure 10). The logical pulse from the FEE is fed to the FPGA, which generates the respective address read-out by the DPU. All data accumulations and consecutive data processing are performed by the DPU.

3.3. Neutral Particle Detector (NPD)

The NPD consists of two identical detectors, each of which is a pinhole camera. Figure 13 provides a conceptual view of one detector and also indicates how the azimuth and elevation angles are defined relative to the overall instrument geometry. In each detector the charged particles, electrons and ions, are removed by the deflection system, which consists of two trapezoidal plates separated by a 3.0 mm gap. In the normal operational mode a 10 kV potential (±5 kV) is applied to the plates and the resulting strong electric field sweeps away all charged particles with energies up to 70 keV. The deflector also collimates the incoming beam in elevation angle. The collimated ENA beam emerging from the entrance 3.0 × 4.5 mm pin-hole hits the START surface with a 15° grazing angle and causes secondary electron emission. By a system of collecting grids, the secondary electrons (SE) are transported to one of two MCP assemblies, producing the START signal for TOF electronics. Depending on the azimuth angle, the collection efficiency varies from 80 to 95%. The incident ENAs are reflected from the START surface nearly specularly. Since the charge state equilibrium is established during the interaction with the surface, the emerging beam contains both the neutral and ionized (positive and negative) components. To increase the total efficiency, no further separation by the charge is made. As proven by ion ray-tracing, there is very little disturbance of the reflected atomic ions leaving the START surface with an energy above 80 eV introduced by the START electron optics. Figure 14 shows the results of electron

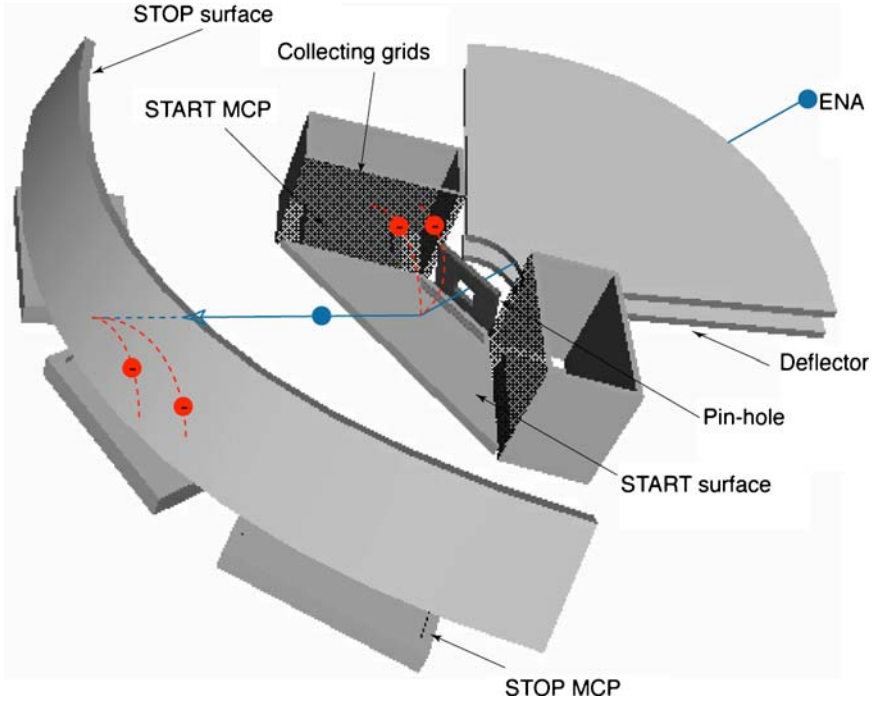

Figure 13. Three-dimensional view of the NPD principal components.

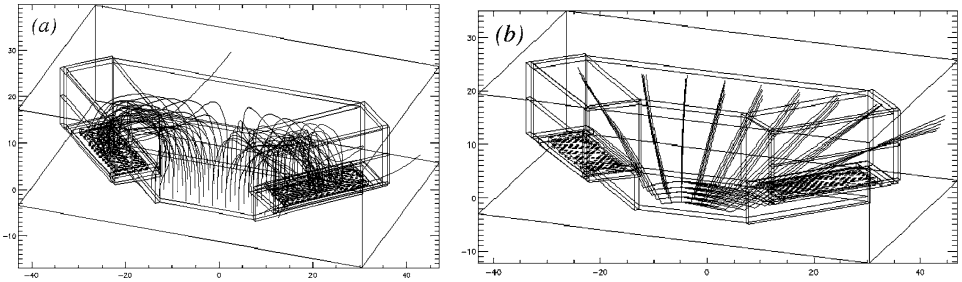

Figure 14. The ray-tracing of the electron (a) and 80 eV ion trajectories (b) in the START NPD assembly electron optics.

and ion ray-tracing in the START electron optics assembly. Therefore particles of all charge states – negative, neutral, and positive – will impact the second surface, the STOP surface. Again secondary electrons will be produced which are detected by one of the three MCP assemblies, giving the STOP signal. The time of flight over a fixed distance of 8 cm defines the particle velocity. Three STOP MCPs also give crude resolution over azimuth to be within the NPD 90° acceptance angle. Since the SE yield depends on mass for the same velocity, the pulse height distribution analysis of the STOP signals can provide the estimation of the ENA mass.

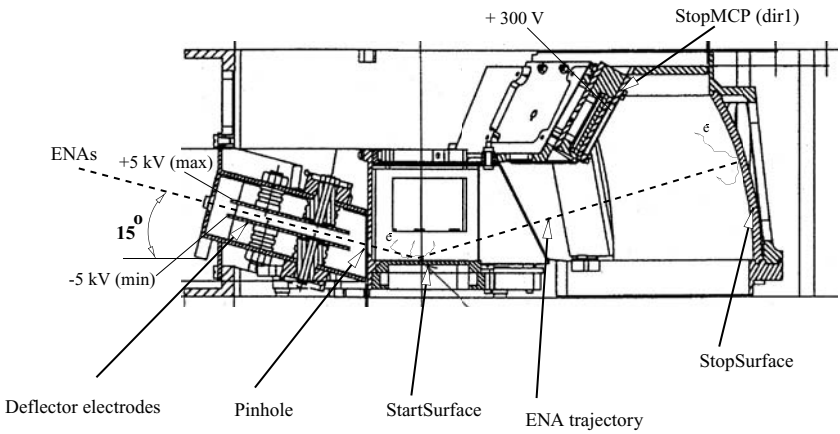

Figure 15. Cross-sectional view of the NPD sensor. The deflector and the STOP MCP front voltages are identified.

Fortunately, the difference in TOF between hydrogen and oxygen is sufficient for direct mass identification within the energy range in question. The accumulation time is commandable, but normally 1 s.

Figure 15 shows a cross-section of the NPD sensor and its main elements. Figure 16 shows different views of the NPD flight model. Two identical sensors are built in a package and installed on the scanner. The NPD package provides 180° coverage, and when combined with the motion of the scanner, 2π coverage (see Figure 5). In order to minimize the sensor mass, all sensor elements are fixed to the outer shell of the mechanical structure. When both sensors are mounted together, electrical screening between units is provided by a kapton film with conductive coating.

The selection of the START and STOP surfaces was the most challenging part of the NPD development. Extensive studies have been performed at University of Bern (Jans, 2000) and Brigham Young University (USA) to optimize the performance of the surfaces which must satisfy a number of requirements, namely, high secondary electron yield, high UV absorption even at grazing angles, high particle reflection coefficient (START surface), low angular scattering, and low photoelectron yield. For the START surface, a multi-layer coating composed of a thin layers of Cr_2O_3, covered by a thicker layer of MgF, and topped with a thin layer of WO_2 was used. The coating was optimized for the absorption of the 121.6 nm line at a 15° incident angle. The reflection coefficient was about 30%, a factor of 2 lower than the uncoated surface. The coating was applied on a titanium substrate polished down to 100 Å roughness.

The STOP surface is graphite (roughness around 100 nm) covered by a MgO layer of about 500 nm. This combination has a very high secondary electron yield, low photoelectron yield, and high UV absorption. Much effort has been expended

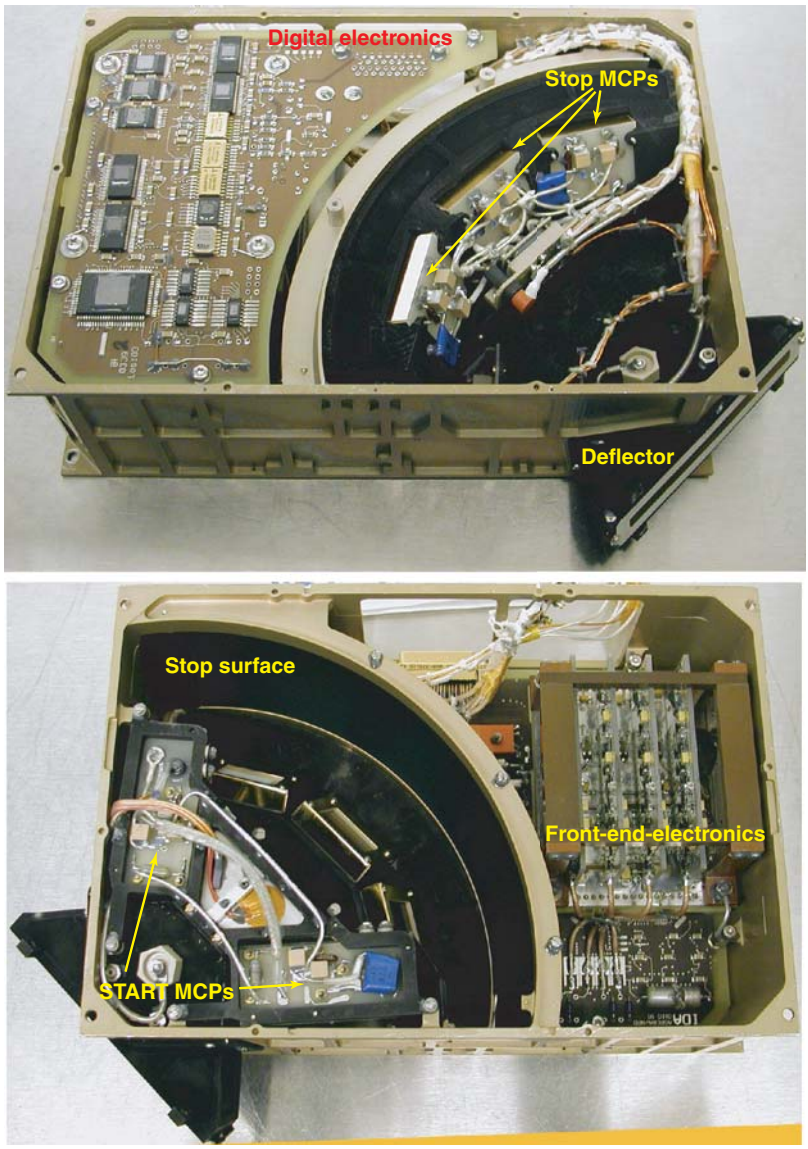

Figure 16. The NPD flight model with the main elements shown.

into increasing the stability of the MgO coating against moisture absorption. It was established that polishing the graphite down to the roughness of around 100 nm improves the surface stability such that no problems related to surface performance (such as possible surface property changes due to increases in the absorption of air humidity during storage and pre-launch operations) are encountered. Thus, the surfaces did not require special maintenance to retain their stability. The importance

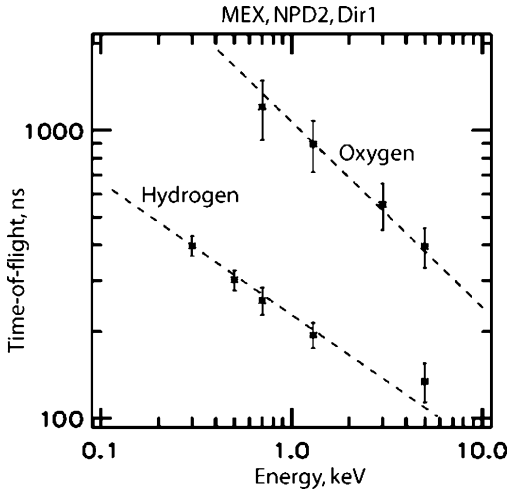

Figure 17. NPD laboratory calibrations: time-of-flight for different masses as a function of energy. The dashed lines give the theoretical dependence corresponding to the 33% energy loss on the START surface.

of achieving this goal was that the surface properties did not change from their calibrated state.

The NPD calibrations included determining the sensor efficiency, total geometrical factor, angular response, and energy resolution. The calibration results fully correspond to the specified performance. Since charge – equilibrium is established in just over a few Å along the parth of the material, a particle interacts with an ion beam can be used for calibrations of ENA sensors. Figure 17 shows the dependence of the measured TOF on the incoming particle energy for protons and H_2O^+. The dashed lines show the theoretical dependence corresponding to the 33% energy loss in the START surface. In the ion source, the produced ionic water molecules break-up during the impact and the residual components carry the same initial velocity as the ion beam, corrected for the energy loss in the target. Therefore, water can be used to calibrate the instrument response to oxygen. Since the TOF for oxygen with an energy below 2 keV is longer than the TOF corresponding to slowest protons at around 100 eV, TOF measurements alone can be used to identify the particle mass (at least in the low energy range).When examining the TOF of both oxygen and hydrogen, it was found that the slopes of the atoms, energy versus TOF are slightly different. The reason for this could be a slight dependence of the reflection properties of the START surface (and thus the effective TOF length) on mass; however, this is only speculation and the true cause remains unknown. Note that, this effect was not observed during calibration of the similar ASPERA-4 NPD.

A 3 keV proton beam was used to generate Figure 18 which shows the NPD angular response over azimuth and elevation for the three STOP sectors, central

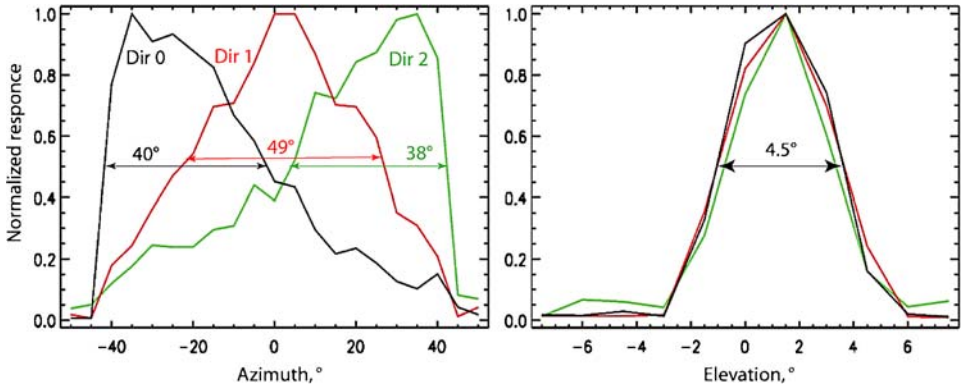

Figure 18. The angular response of the NPD 2 sensor over azimuth and elevation.

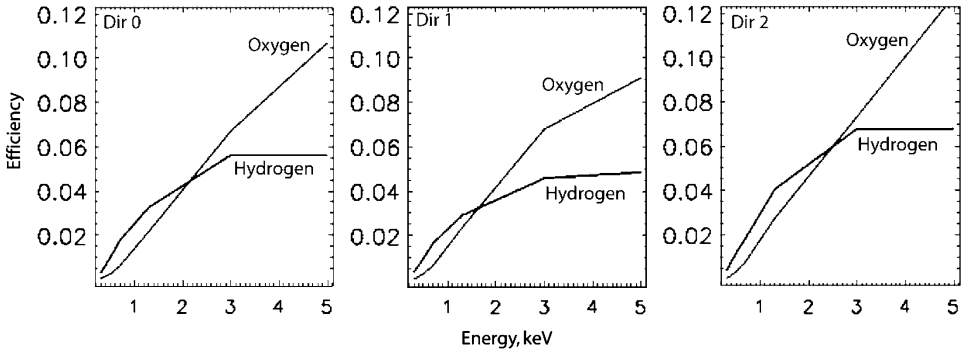

Figure 19. The NPD2 sensor absolute efficiency for oxygen and hydrogen ions (atoms).

(red) and two side (green and black). The FWHM varies over azimuth from 49° for the central sector to 38° and 40° for the side sectors. The FWHM is constant over elevation, 4.5° for all directions. The difference in the azimuthal response for different directions is a geometrical effect; particles from the side direction have a lower probability of reaching the STOP surface. In addition, the STOP and START secondary electron collection efficiency is lower due to fringe field effects.

Figure 19 shows the absolute efficiency of the NPD sensor as a function of energy for proton and H_2O^+ (oxygen) beams. As seen on the graph at 5 keV, the efficiency is more than 10% for oxygen ENAs, and the efficiency reaches 5–6% for hydrogen ENAs. Up to a certain energy, the efficiency increases with energy corresponding to an increase in the secondary electron yield on both START and STOP surfaces. At the energy where the yield exceeds the unity on both surfaces, the efficiency levels out (ca. 3 keV for protons and 6 keV for oxygen). At energies below 1 keV, the efficiency is around a few percent.

Each NPD sensor is an "intelligent" device and its electronics perform a substantial portion of the data pre-processing. The NPD electronics consists of two boards:

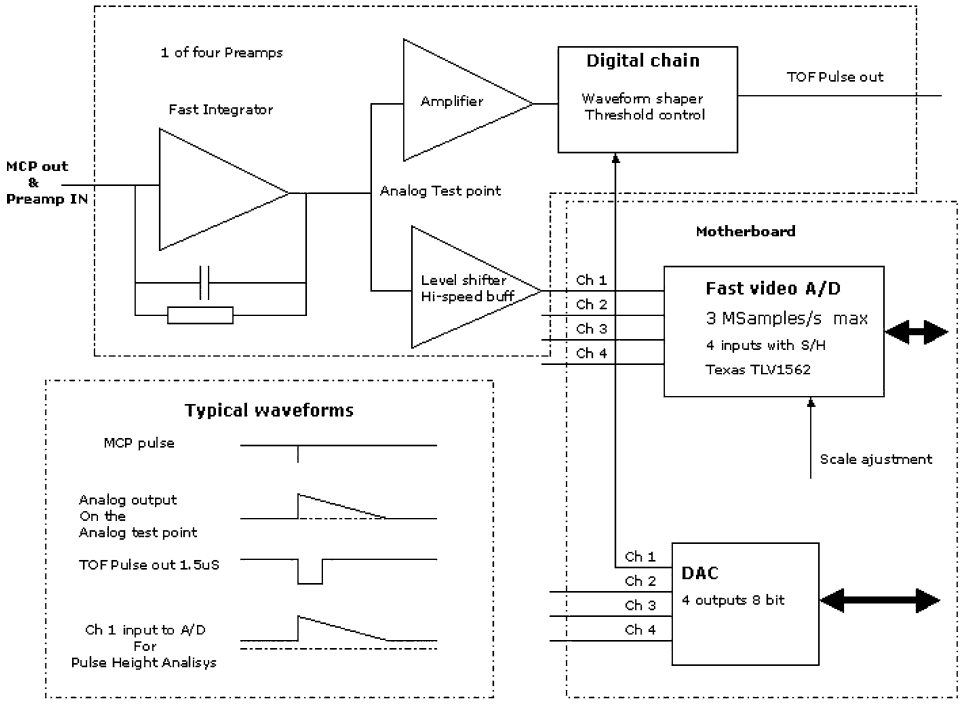

Figure 20. NPD FEE (Front End Electronics) block diagram.

FEE and digital TOF electronics (DigTOF). All high voltages are provided and controlled externally. The FEE block diagram and typical signal shapes are shown in Figure 20. Pulses from four MCP anodes (one START and three STOPs) are fed to fast MOS FET – based discrete charge sensitive preamplifiers (frequency cut-off at 6 GHz) which is followed by operational amplifies. The wave shaper generates a fast logic pulse for the Time-To-Digit converter (TDC) of the DigTOF board and fast video ADC Texas TLV1562 (Analog-To-Digital converters) performs pulse height analysis. The signals are up shifted by 0.8 V to reach the ADC working range of 0.8–3.8 V. Four DACs (Digital-to-Analog converters) provide threshold control. The thresholds are commandable. FEE provides theoretically a TOF resolution of 0.1 ns that is much below what is required for this measurement technique. Even a resolution of 1 ns would be sufficient.

The DigTOF electronics serves a number of tasks including TOF measurements from one START to one out of three STOP signals, serving FEE and initiating analog to digital conversion of STOP pulses, coincidence check and selection of valid TOF STOP pulse height pairs, counting events, buffering three different data types in SRAM (Static RAM, Random Access Memory), and interfacing DigTOF to the DPU. Figure 21 shows the DigTOF block diagram focused on the functionality of the diffirent componets and FPGA subroutines. The occurrence of a START

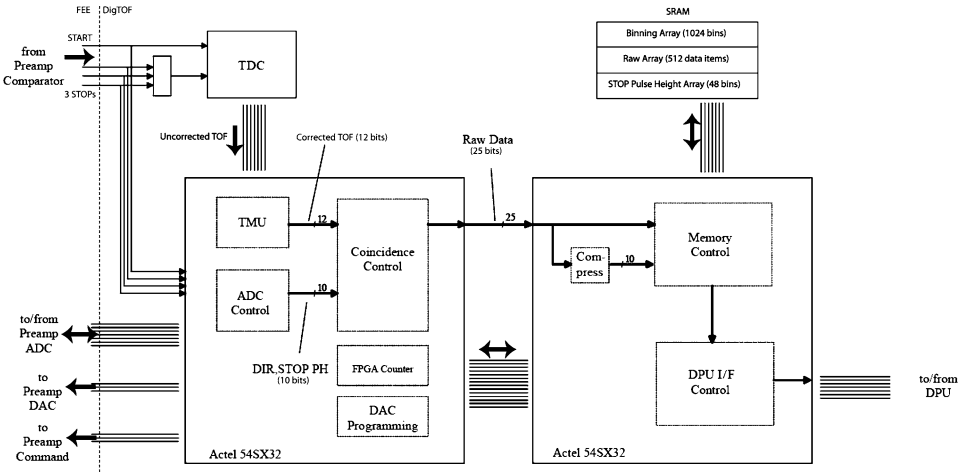

Figure 21. NPD DigTOF (Digital TOF electronics) block diagram.

signal, followed by a STOP signal leads to a TOF measurement in the TDC and generation of a data item with uncorrected TOF information. The obtained time is then corrected to compensate for a possible temperature shift. The calibrations are performed continuously using 6 MHz clock supplied by the DPU and the calibration constants at DigTOF are continuously updated. The TDC control and TOF correction are performed by a TDC Management Unit (TMU), a part of FPGA. The final time data item is a TOF value with 12-bit binary time information. In parallel to this, a sampling process by FEE ADC follows the occurrence of a STOP signal, thus a 10-bit data item with information of both direction and 8-bit STOP pulse height is generated. The coincidence control then checks for a valid coincidence of these two data items and additionally flags the occurrence of more than one START or STOP signal during TOF measurements. This now leads to a 25-bit raw data item that is used for the pending storing process. The memory control has to handle three different memory areas in the SRAM. For the binning array, the raw data is compressed into 10-bit data that represents the bin number inside the array. The respective bin is incremented by one up to the bin depth of 65,536 (16 bit). For the raw data array, incoming raw data items are successively stored until this array is filled completely (512 entries). The STOP counter array is filled in the same way as the binning array, but with the compressed STOP pulse height together with the respective direction. All data arrays are filled in parallel (binning array is excluded, if coincidence level does not fit). Readout and the following initialization of these arrays are performed by using burst read access from the DPU. Besides the STOP counter array, 16-bit event counters and two registers facing the preamplifier board are implemented in FPGAs. One of these registers is used to program FEE DACs, the other for directly commanding FEE. All control, counter, and memory data are

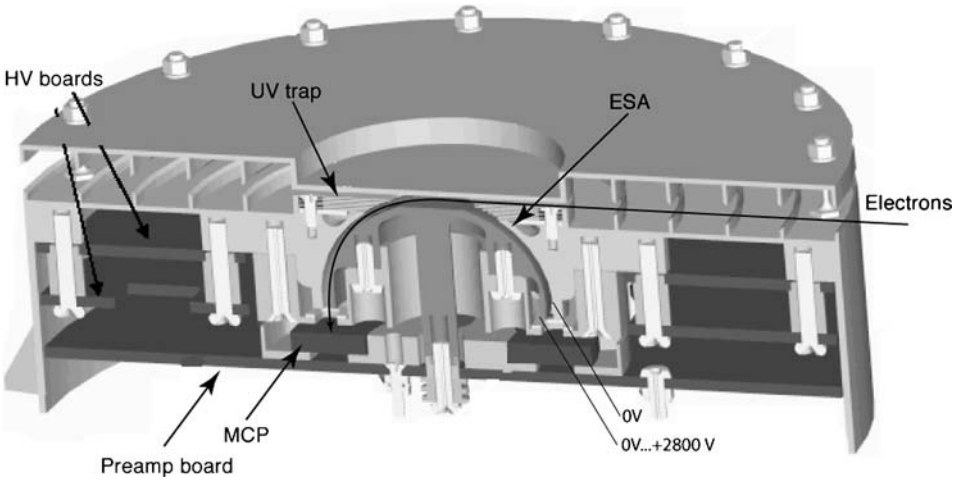

Figure 22. Cut-sectional view of the ELS sensor. The electrostatic analyzer voltages are also indicated.

accessed from the DPU over 16-bit registers; physically the connection to the DPU is a 16-bit bus. DigTOF is realized in two FPGA Actel 54SX32.

3.4. Electron Spectrometer (ELS)

The ELS sensor represents a new generation of ultra-light, low-power, electron sensors (Figures 22 and 23). It is formed by using a collimator system followed by a spherical top-hat electrostatic analyzer (Sablik *et al*., 1990), achieving a geometric factor of 5.88×10^{-4} cm^2 sr. The top-hat has a 17° opening angle and a 90° turn angle. The radii of the inner and outer hemispheres are 14.9 and 15.9 mm, respectively. Particles enter the aperture at any angle within the "plane" of incidence, which is determined by the collimator to be $4° \times 360°$. Electrons are then deflected into the spectrometer by applying a positive voltage to the inner hemisphere. The electrons hit an MCP after being filtered in energy by the analyzer plates. There are 16 anodes behind the MCP, each anode defining a 22.5° sector and each connected to a preamplifier. Each ELS preamplifier generates TTL signals, which are then counted by the DPU. ELS deflection plates are stepped in voltage sequences to achieve differential spectral measurements. Electrons with energies up to 20 keV/q can be measured.

The ELS unit has a self-contained, dual range, linear power supply. The first power supply range is from 0 to about 21 V (about 150 eV) and has 4096 possible settings. The second power supply range is from 0 to 2800 V (about 20 keV) and also has 4096 possible settings. The ELS sweep is fully programmable within the constraint that the maximum decay rate is 32 steps/s. On any given step, the deflection plate voltage is held constant during a minimum of 28.125 ms, which

Figure 23. ELS spare (*left*) and flight models (*right*).

is used to accumulate electrons. There is a minimum of 3.125 ms of data latency between energy steps for transition. Thus, the total time per energy step is 31.25 ms.

The ELS FEE (similar to NPI) generates outputs from 16 anodes which are fed through individual amplifiers housed in two MOCAD chips. These amplifiers convert and amplify the MCP pulse into a TTL signal which is sent from the sensor through communication lines (16) to the DPU. The DPU gathers the samples and controls the accumulation time for the step, as well as the latency between steps and the energy sweep. The DPU also controls the instrument settings and determines when to read the monitor outputs. The ELS sensor is mounted on top of the NPI sensor, which is mounted on top of the DPU as an assembly. This assembly is mounted on the ASPERA-3 scan platform (Figure 5) in such a way that the full 4π angular distribution of electrons is measured during each platform scan (the scanner takes 32, 64, or 128 s to complete a sample rotation).

ELS was designed to be solar blind so that it may operate in exposure to direct sunlight. This has been achieved by using two UV reducing mechanisms and one secondary electron suppression technique. UV is minimized through the use of a series of light baffles in the ELS collimator and a series of UV light traps at the entrance to the spherical deflection plates. Secondary electrons are reduced by the addition of a special coating, based on a modified Ebanol-C process, which is included throughout the deflection surface, light trap, and collimator system (Johnstone *et al.*, 1997). To avoid overload of the MCP by photoelectrons, a grid is installed in front of the MCP assemblies, which can be biased by a voltage (256 programmable) in the range from 0 V to -5 V.

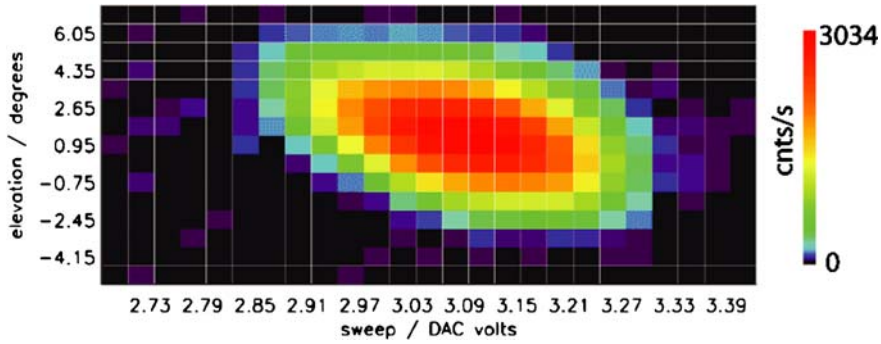

Figure 24. ELS calibrations: Typical spectrograph of the elevation angle versus the applied voltage on the inner hemisphere (100 eV beam, sector 7).

ELS was calibrated at the Mullard Space Science Laboratory (MSSL) in the United Kingdom. The calibration facility (Johnstone *et al*., 1997), based on the technique described in Marshall *et al*. (1986), provides a wide area photoelectron beam at energies ranging from a few eV to 15 keV with variable beam intensities from a few Hz to several MHz. The system is fully automated facilitating calibration scans over the complete range of polar and azimuth angles at several instrument voltage settings both for the analyzer as well as the MCP. A flexible data acquisition system was integrated into the automation to provide simultaneous measurements from the 16 preamplifier channels, coordinated with the instruments position and voltage settings. Before performing the instrument calibration, a profile of the beam output is recorded at each of the calibration energies by means of a channel multiplier mounted on an X-Y table. During calibrations, the channeltron is mounted as close as possible to the instrument aperture in order to provide a constant reference to the beam intensity.

The instrument has two operational voltage ranges for the energy sweeps as described earlier, and hence, tests were carried out at several energies in both ranges to cover $\pm 180^\circ$ in polar and $\pm 3^\circ$ in azimuth. Figure 24 is a typical plot of the voltage-angle scans carried out over sector 7 using a 100 eV electron beam (similar for other sectors). Such plots were used to calculate the k-factor factor (central energy/analyzer voltage) of the analyzer and energy resolution for all 16 sectors. Figure 25 is a plot of the k-factor across the 16 anodes. Although the k-factor is lower than the design value of 7.5 eV/V, the variation across the anodes is less than 10%, allowing small deviations in the instrument response to be determined from good calibrations. The calibrations also established the initial MCP operational level for flight (2250 V).

Finally, calibration of ELS also tested the UV rejection ratio of the analyzer using a Lyman α UV source (Alsop *et al*., 1996). Figure 26 shows the rejection efficiency versus analyzer voltage for sector 5 with the screen grid on and off (these

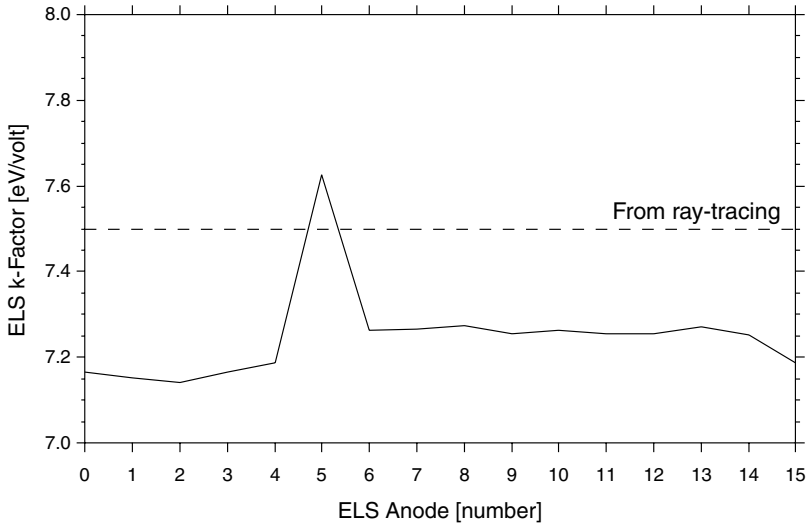

Figure 25. ELS calibrations: variation in *k*-factor (central energy/analyzer voltage) across the 16 anodes.

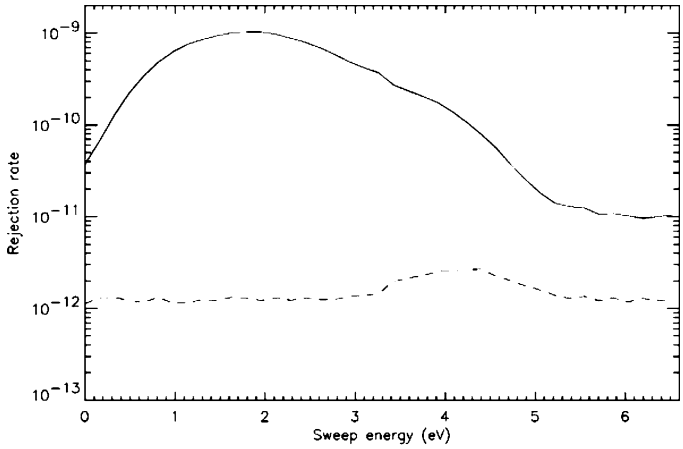

Figure 26. ELS calibrations: UV rejection (summed over all elevations) versus sweep energy for sector 5 (*solid line*: grid off, *dashed line*: grid on).

data are typical for all other sectors). When the grid is on, photoelectrons produced inside the analyzer are effectively repelled, which results in a decrease of the UV related signal by a factor of almost 1000.

ELS is operated in several modes with different sweeps. The most common mode is a survey mode where the ELS sweep steps through 128 of its possible 8192 voltage settings in 4 s to produce a logarithmic energy sweep covering the full ELS energy range (to 20 keV). Adjacent energy steps coincide at about the 50% point

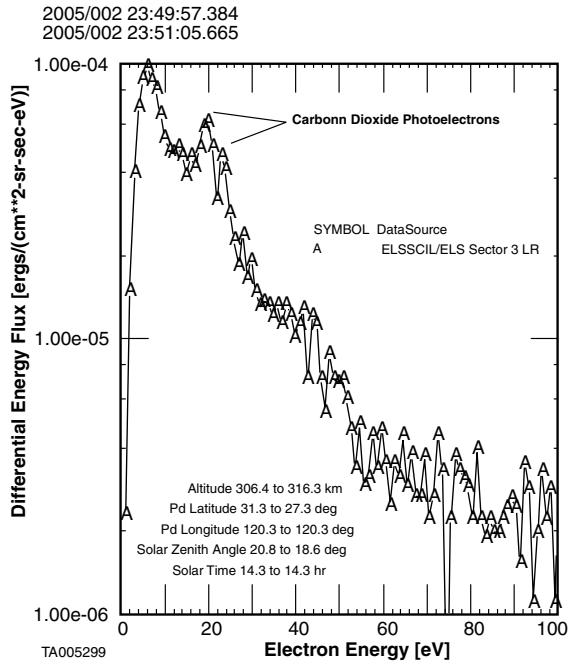

Figure 27. ELS measurement at Mars: photoelectron spectrum from the Mars ionosphere.

of the sector response. In this mode, energy and/or time degradation is selectable, but is seldom used.

ELS is sometimes operated in a linear stepping mode which produces an oversampled spectrum of 128 selected voltage settings every 4 s. Here, the energy width of a sector is usually larger than the center energies between steps. When combined with the knowledge of the instrumental response function, flux values can be adjusted to account for measurement overlap of the same parent function by removing the overlap flux, and thus sharpening the measurement (Early and Long, 2001). Electron measurements from this linear stepping mode are shown in Figure 27, which shows that ELS can resolve of the CO_2 photoelectron peaks, characteristic of the Martian atmosphere.

Since ELS is fully programmable, there are energy modes defined which select randomly sampled energies, and other modes which alter the time for the sweep resolution and number of samples in a sweep. The minimum requirement for programming the ELS energy sweep is that there can be no more than 32 energy steps per second and a change between voltage levels of 10% requires a 3.125 ms dead time for the ELS power supply to settle to the new deflection value (factor of safety is 3 for dead time). ELS will take advantage of its programming capability to best sample Martian phenomena.

3.5. Ion Mass Analyzer (IMA)

IMA is a stand alone instrument with its own DPU and high voltage power supplies (Figure 5). The ASPERA MU only provides the required voltages (+5 V, −5 V, +12 V, and −12 V, +30 V) and serves as a relay for IMA telemetry (TM) packages. The IMA instrument comprises a sensor, high voltage supply, and a DPU with housekeeping electronics which interface the sensor and the ASPERA-3 DPU.

3.5.1. *IMA Sensor*

The IMA sensor consist of four main components: electrostatic deflection system to provide elevation sweep, top-hat electrostatic energy analyzer, permanent magnet-based velocity analyzer, and an MCP detector with a position sensitive anode (Figure 28). Ions enter the sensor through a grid grounded to the spacecraft such that the entrance grid is at the spacecraft potential. Behind the grid is a deflection system which has the purpose of sweeping the elevation acceptance angle between 45° and 135° with respect to the symmetry axis. Particles passing the deflector continue into a spherical 127° top-hat electrostatic analyzer (ESA). The dimensions of the ESA are 45.0 mm (center radius) and 2.2 mm (gap between the two plates). The outer hemisphere of the analyzer is kept at a fixed low voltage (−100 V), while the inner hemisphere is stepped through the high-energy part of the voltage sweep, from −4 kV up to −100 V. During the lower energy portion of the sweep

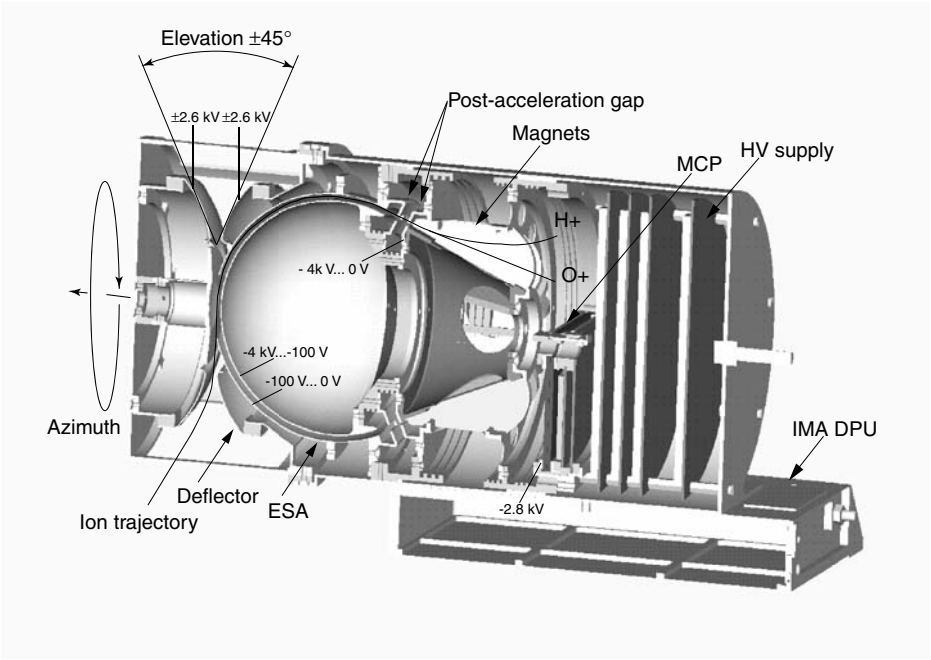

Figure 28. The IMA instrument cross-section. The key voltages are identified.

the situation is reversed, the inner hemisphere is kept at a fixed potential and the potential on the outer hemisphere is stepped up towards ground potential. That allows more accurate (closer energy steps) and precise (lower voltage setting error) measurements in the low energy range. Ions transmitted through the ESA pass through a two-slit electrostatic lens consisting of a 7 mm slit (closer to ESA) and a 1 mm slit (closer to the magnetic section). The size of the slits is a compromise between mass resolution and the instrument sensitivity. The mass analyzer uses a circular magnetic field, which deflects the ions outward, away from the central axis of the analyzer system. The magnetic system consists of 16 radially oriented permanently magnetized neodymium-iron-boron magnets (VACODYM® alloy). To lower the stray magnetic fields, the 16 magnets are matched to have the same magnetization within $\pm 1\%$ accuracy. The magnetic field strength is approximately 1200 G in the center of the section. The entire magnet assembly can be biased by a post-acceleration voltage between 0 and -4 kV. The post-acceleration is used to vary the mass resolution of the instrument. Low post-acceleration increases the mass resolution due to an increasing difference in the gyroradius between different masses, although low energy protons cannot be detected because they impact the analyzer walls due to the small gyroradius. Protons with energy below 1 keV require the maximum post-acceleration to reach the detector.

Particles striking the front of the 100 mm diameter MCP (two stacked plates biased on the front at -2.8 kV and with a 300 V drop between the MCP back and the anode) produce an electron cloud of approximately 10^5–10^6 electrons. The electron cloud is split between rings and anodes of the IMA position sensitive detector. A system of 32 concentrically spaced anode rings behind the MCP measures the radial impact position (representing ion mass), whereas 16 sector anodes measure the azimuthal impact position (representing the ion entrance angle). The 32 ring anodes and the 16 sector anodes are each connected to 6 charge-sensitive MOCAD preamplifiers (8 channels per chip). When the preamplifier TTL output of both a ring and a sector is high, coincidence circuitry implemented in an FPGA resolves the impact coordinates. The coordinates are used by another FPGA to update a 32 by 16 memory position matrix (16-bit deep) with one count every time a valid particle is detected in a given ring-sector (mass-angle) position. Two memories are used to allow for double buffering of data. While data is being accumulated into one memory, the IMA DPU reads the other memory.

Internal working mode of the IMA sensor is always the same. The fastest changing parameter is the particle energy. It sweeps from 36,000 eV down to 10 eV over 96 logarithmically equidistant steps. The sampling time on the each energy step is 125 ms. The "mass image" of 16 azimuthal sectors $\times$ 32 rings (mass) is read-out once per sampling time. After each complete energy sweep the instrument changes the polar angle of the field of view. The polar angle scans from -45° up to $+45^\circ$ over 16 steps. The total time to complete a 3D spectrum is 192 s. This spectrum consists of 32 rings (mass) $\times$ 16 azimuthal sectors $\times$ 96 energy steps $\times$ 16 polar angles.

3.5.2. *IMA Electronics and Data Processing Unit*

The IMA electronics includes high voltage power supplies for biasing of the various electrostatic filters and the MCP assembly, and digital electronics to handle the instrument operations. The high voltage supplies are laid out on two circular boards in the cylindrical sensor part of the instrument (Figure 28). The high voltages are achieved by switched-mode power supplies converting an input voltage of 25–30 V DC to approximately 4500 V DC through the use of transformer ratios and subsequent chains of diode-capacitor voltage multipliers. IMA has two separate high voltage power supplies. One supply is dedicated to keeping the front side of the MCP biased to -2.8 kV, while the other supply generates all other high voltages as fixed "raw" voltages. These raw voltages are then regulated by the use of high voltage optocouplers (Amptek HV601B). The electrostatic entrance filter can be stepped between ± 2.6 kV to an accuracy of 1.2 V using a 12-bit DAC and the electrostatic energy filter is stepped between 0 and -4.0 kV also using an 8-bit DAC with a high voltage optocoupler. As described above, high accuracy at low voltage settings is achieved by fixing the -4.5 kV supply at a voltage of about -100 V, and using a -100 V supply with a 12-bit DAC connected to the outer ESA hemisphere to step through the lower energy range. The post-acceleration voltage is also taken from the raw -4.5 kV voltage and set to the desired voltage using an optocoupler.

The IMA DPU is built around a 16-bit processor (MA31750) and performs the following main functions: (a) reading of data from the double-buffered sensor memory and processing of the data, (b) feed the IEEE 1355 digital serial interface to the MU DPU with processed and formatted data, (c) receive commands on the serial interface from the MU DPU, (d) control the high voltage power supplies' settings and monitor voltages and temperatures. Data processing includes three steps (1) summation (if commanded) of the angle bins (azimuth/elevation) and/or mass bins, (2) logarithmical compression of the count values from 16 to 8 bits, (3) loss-less RICE compression of the final spectrum. The mode of the processing is set by a telecommand (TC) or chosen automatically according to telemetry rate limitations. The post-acceleration level is changed by a TC. Only 3 values of the post-acceleration are available: 0 V, -2150 V, and -3650 V. Due to the data compression, the output data packets have variable length, and are buffered until enough compressed and time-stamped packets are available to fill a fixed length packet transmitted to the MU. To improve the compression efficiency a fixed background level can be subtracted onboard. Directions shadowed by the spacecraft can be masked out to avoid sending data which are not valid.

3.5.3. *IMA Calibrations*

IMA calibrations were performed at Centre d'Etude Spatiale des Rayonnements, Toulouse, France (Figure 29). Before calibrations IMA was extensively ray-traced and the model was then verified against the calibrations. That allowed minimizing the calibrations and calibrating only individual sectors. During the calibration the

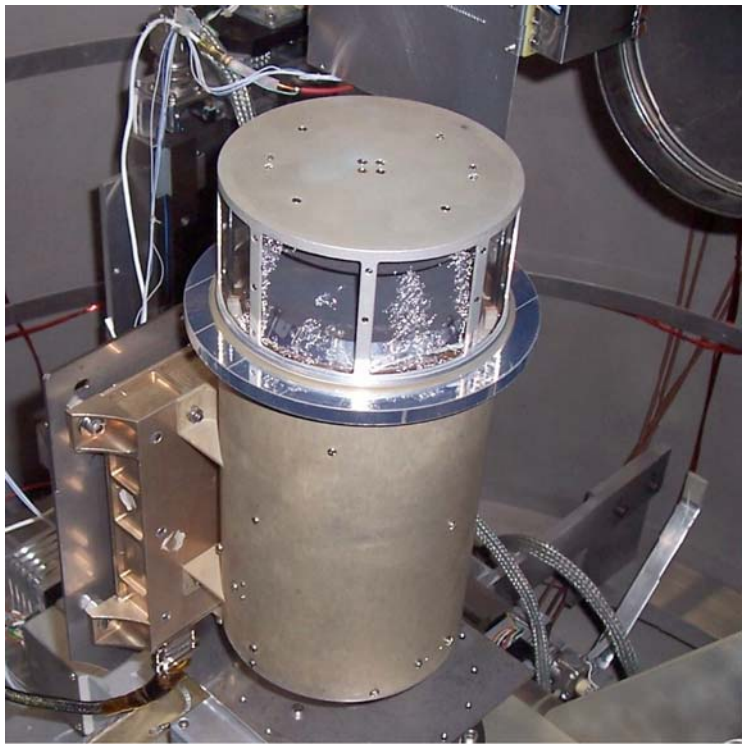

Figure 29. The IMA instrument in the vacuum chamber during calibrations.

full response function was defined for selected masses. Figure 30 demonstrates the IMA angular responses: the instrument's effective aperture (in cm^2) as a function of the elevation angle for a fixed azimuth at the maximum response (a), and the azimuth response for a fixed elevation at the maximum response (b). Despite the ion optics can provide the azimuth resolution down to 15° (FWHM), the instrument resolution defined by the full field of view divided by 16 sectors is assumed to be 22.5°. As expected the mass resolution strongly depends on the post-acceleration voltage (Figure 31), but even at the maximum post-acceleration value, IMA can resolve amu/charge = 1, 4, 14. For the incoming beam energy of 1.2 keV, the proton peak is observed to disappear below $V_{\text{postacc}} = -2000$ V while at sufficiently high post-acceleration voltages, all masses can reach the detector. At the medium post-acceleration, $V_{\text{postacc}} = -2000$ V, the mass resolution of IMA is sufficient to resolve all masses relevant to the near-Mars space (Figure 32). The calibrated curves of the constant mass in the energy-mass matrix are in excellent agreement with the observations at Mars. Figure 33 shows the energy-mass matrix for $V_{\text{postacc}} = -2000$ V accumulated by the IMA sensor for 1.5 years at Mars along with the theoretical mass lines. The yellow band at about 700 eV is a contamination from the solar wind protons.

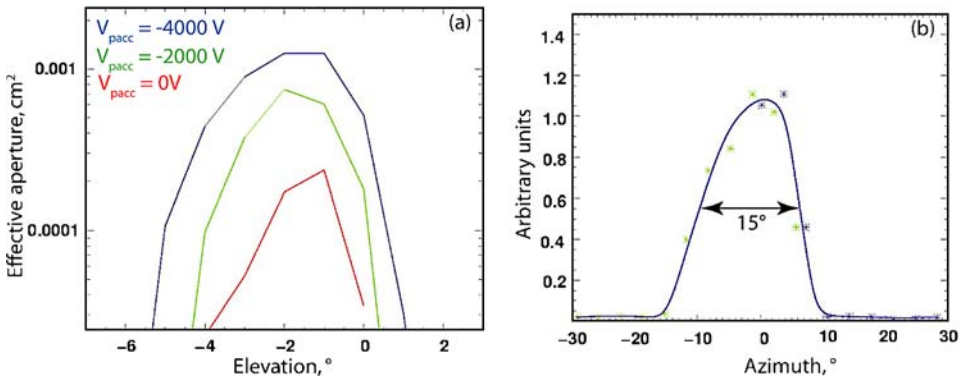

Figure 30. IMA angular response over elevation for different post-accelerations (V_{pacc}) and azimuth.

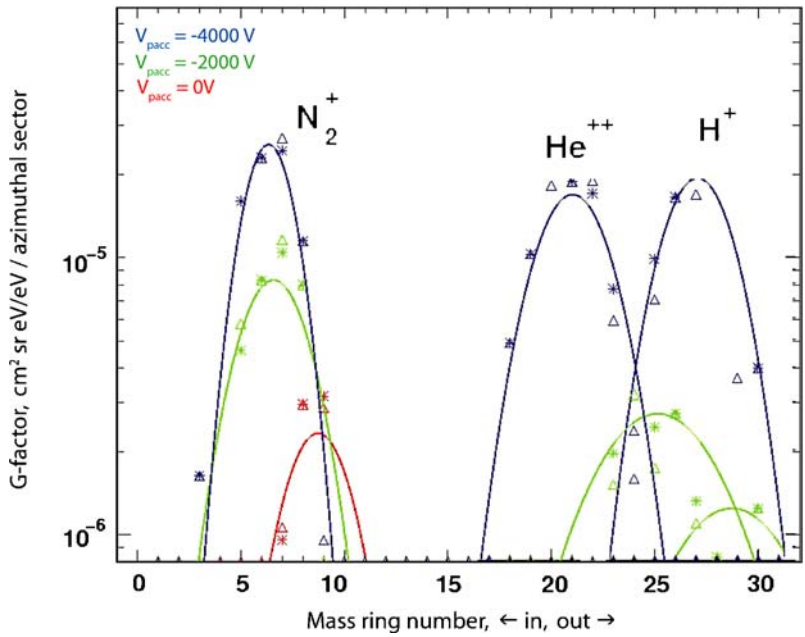

Figure 31. IMA mass resolution for different post-acceleration voltages. The beam energy is 1.2 keV.

3.6. SCANNER

The scanner platform was originally developed as part of the ASPERA-C experiment during the Russian Mars-96 project. Some modifications were made for the ASPERA-3 on Mars Express, most of them concerned optimization of the performance during long-term operations and reduction of its mass. The scanner, shown in Figure 34 and technical characteristics are given in Table IV, constitutes the 0° to 180° rotating platform on which the sensors (ELS, NPI, NPD1 and NPD2) as

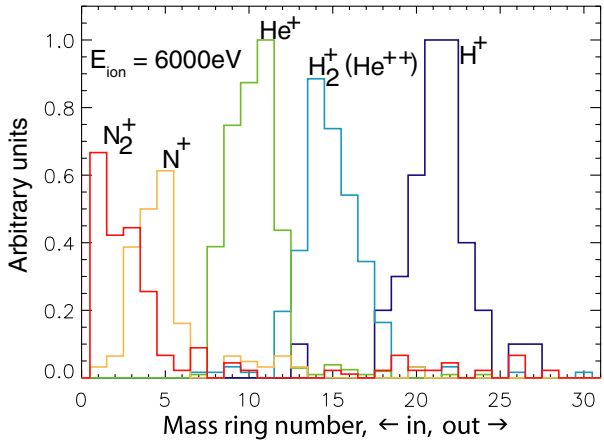

Figure 32. IMA mass resolution for 6 keV particles and $V_{\text{postacc}} = -2000$ V.

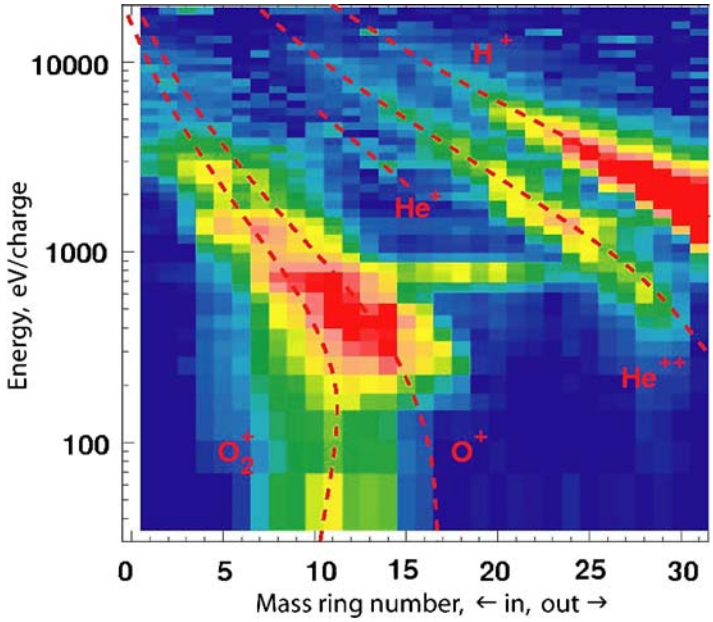

Figure 33. Energy – mass matrix for $V_{\text{postacc}} = -2000$ V, accumulated by the IMA sensor for 1.5 years at Mars with the theoretical mass lines. The yellow band at about 700 eV is a contamination from the solar wind protons.

well as the DPU, high voltage power supply, house keeping and DC/DC boards are situated. The scanner provides all necessary mechanical and electrical interfaces between the spacecraft and ASPERA-3. Rotation is accomplished by the use of a worm gear mechanism, which was selected in order to minimize friction, and

TABLE IV
Scanner technical characteristics.

Parameter	Value
Maximum angle of rotation (°)	±100
Angular movement per step (°)	0.0095–0.0190
Angular position feedback resolution (°)	0.05
Angular positioning accuracy (°)	0.2
Operational rotation rate (°/s)	1.5/3.0/6.0
Maximum rotation rate (°/s)	∼25.0
Power dissipation (W)	0.5–2.0
Platform load (kg)	3.7
Maximum platform load (kg)	∼12
Dimensions (mm)	60 × 254 × 232
Mass (kg)	1.42
Operational lifetime in vacuum (years)	∼3
Gear ratio	188

Figure 34. The ASPERA-3 scanner.

obtain a high gear ratio (1:188). The scan platform is made as a plug-in unit for the sensor assembly. Considerable efforts were spent to reduce mass, volume, power consumption, and out-gassing in vacuum as well as to achieve high reliability.

We have not made any particularly investigations to measure the level of microvibrations induced by the scanner motion since the scanner does not have any

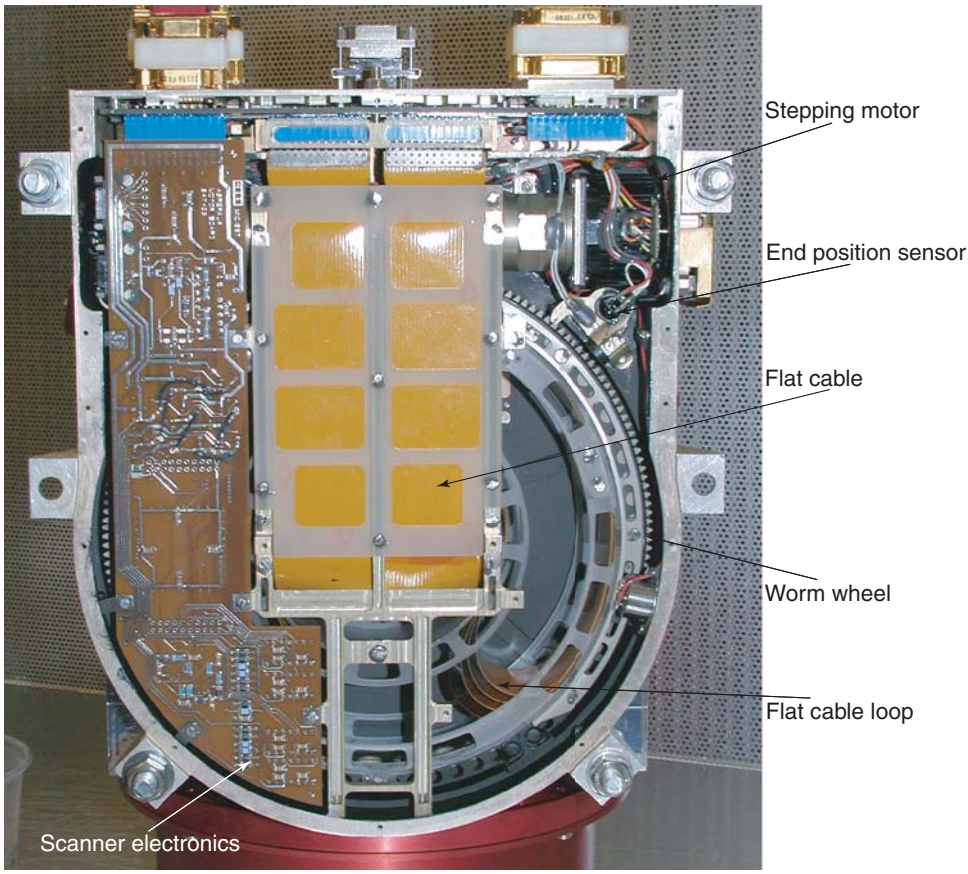

Figure 35. Scanner interior with the main features identified.

parts moving with high frequency. What might be a problem are extremely small changes in the spacecraft attitude caused by the Main Assembly motion and the associated onboard attitude control system reaction. The level of the spacecraft attitude changes as given by the Mars Express gyros readings was in the range 0.3 mrad (maximum over all three axes). To illuminate any possible effects on remote sensing instruments the scanner operations were conducted outside their operations.

3.6.1. *Mechanics*

Figure 35 shows the scanner internal view. The large diameter worm wheel to which the sensor assembly is fixed is rotated by a stepper motor *via* a co-axial worm screw (not visible below the flat cable). The worm wheel is fixed to the structure with a large diameter angular contact ball bearing. During the scanner lifetime tests, several types of bearing balls were tested, including the balls originally mounted in the bearings. The bearing balls which were ultimately used are of ceramic type Si_3N_4, which was found to be the best suited to meet the ASPERA-3 requirements.

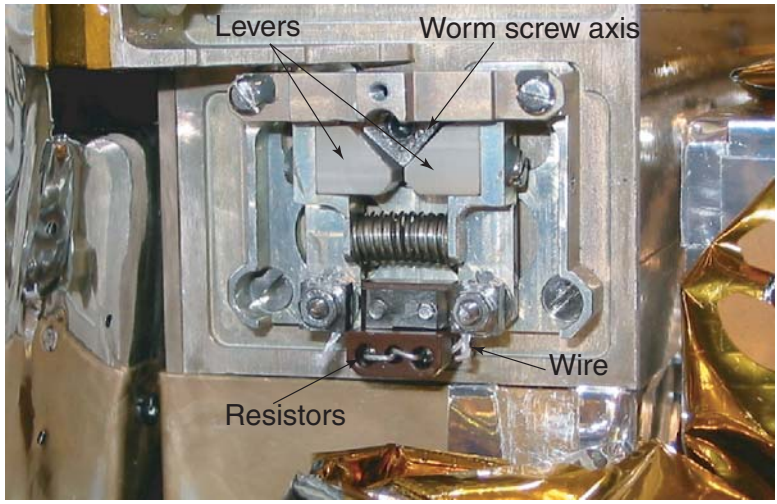

Figure 36. Scanner locking mechanism.

The housing and circular sensor platform is manufactured using a high-strength aluminum alloy. The position of the movable parts relative the scanner is given by three magnetic sensors: two end-sensors at 0° and 180°, and one step counter. Because of the long-term operational requirements, no mechanical contact exists with the sensors. A feed-through cable loop consisting of six flat cables with connectors, each cable with 26 conductors (a maximum of 156 connections possible) interfacing through D-SUB connectors, provides electrical interface to the satellite electrical systems for the entire ASPERA-3 instrument.

During launch and other necessary transports (when the instrument is without electrical power), ASPERA-3 was expected to encounter heavy mechanical vibrational loads. A worm gear type of mechanism provides a self-locking behavior without electrical power, and thus, was selected for use on the scanner. A true locking mechanism was also included on the scanner (Figure 36) and prevents unwanted movements of the platform. This locking mechanism consists of a wire which ties together two small levers, locking the square-shaped worm screw axis. By command, the axis is unlocked by applying a voltage to a resistor which burns the wire and then the levers are forced to move apart by the actions of a spring. The release scanner command can be executed only once.

3.6.2. *Motor*

The stepper motor used is a modified P430 from Escap. The two ball bearings within the stepper motor holding the motor shaft were modified. The original ball bearings are replaced by type NMB R-1350ZZ bearings which have a surface treated with NoWear Gamma by SKF, Sweden. The balls are made of Si_3N_4 (NBD200) by Saint Gobain/Cerbec and have a diameter of 2.00018 mm, grade 5. The ball holders

are designed and manufactured at IRF, Kiruna, Sweden and are made of Beraloy (Acoflon 100 Mo, 97% PTFE + 3% MoS_2). The ball bearings are mounted by IRF, Kiruna, Sweden in the motor with shims for a correct axial displacement. Also, the ball bearings are mounted without any axial tension in order to release the ball bearings from wear. The motor shaft is isolated from any axial load created by the worm screw with a soft split of the motor shaft and worm screw.

In the original design the scanner had two motors (one redundant) and two sets of driving electronics. The worm gear was directly coupled to both motor shafts. While the operating motor was driving the worm gear, the cold back-up motor was a passive mechanical load. However, during life-time test it was found that the cold back-up motor is a potential source of a mechanical failure (jamming). Therefore, only one motor and respective electronics were used in the final design.

3.6.3. *Electronics*

The motor electronics located in the scanner provides motor control and driving. The stepper motor is driven by a classical H-bridge drive system with a motor current control system. The location of the board is shown in Figure 35.

For a smooth stepping of the motor, 16 microsteps per full step and winding are implemented. The 16 microstep levels are set by an ACTEL FPGA to a DAC, both situated on the scanner electronics board and set the current reference value for the motor current control system. In addition to current control, for minimizing mechanical interaction with its environment, the scanner electronics controls the scanner start up sequence by providing a start up ramp. Given a start up command, the scanner electronics ramps up the scanner speed from zero to full speed in 4 steps. In order to increase the torque of the motor, an offset of the current setting can be changed by command. By command, one can also set the coast as well as the ramp current separately, meaning that there can be a higher current (higher torque) during the ramp period than during the coast period.

The following modes of the scanner operation are possible: (1) continuous scanning back-and-forth between 0° and 180° in speed steps of 128, 64 and 32 seconds/180°, (2) continuous back-and-forth scans in steps of predefined by TC degrees and predefined by TC sampling time for each step, (3) positioning in any predefined by TC position. The determination of the scanner position is obtained by counting pulses from the wheel sensor that sits on the motor shaft as it rotates away from one of the two end position sensors. The end sensors reset the pulse counter. The angular positioning accuracy of the scanner pointing direction is 0.2°.

3.7. Main Unit (MU) Electronics

Functionally, the MU electronics includes DC/DC electronics, a high voltage power supply (HVPS), and data processing electronics. The DC/DC electronics is a single board, the HVPS includes two boards in a stack configuration, and the data processing electronics also includes two boards, a DPU board and a housekeeping (HK)

board. The later two are connected together with the sensor control electronics, the power supply, and the HVPS *via* a common bus system with 8 address and 16 data lines besides control, analog and power supply lines.

3.7.1. *Digital Processing Unit (DPU)*

The DPU is built around a 16-bit processor (MA31750 from Dynex) with 12 MHz system clock frequency and an FPGA RT54SX32S, which implements memory management, watchdog functions, and the serial spacecraft interface protocol. The software runs inside a 128 kByte RAM, organized in 2 banks each processing two 32 kByte of static memory chips. On power-up, a two times 16 kByte bipolar PROM (HARRIS) (Programmable Read-Only Memory) is activated with a boot loader, which transfers the complete PROM contents into the RAM, changes the program control to the RAM area, and then switches the power to the PROMs off *via* transistor switches to conserve power. A 512 kByte radiation hardened EEPROM (Maxwell) (Electrically Erasable Programmable Read Only Memory) contains additional program code and configuration information, which can be modified from ground. A 2 MByte mass memory RAM is used to store measurement data and buffer telemetry packets. An Actel FPGA RT1280 implements the serial data transfer protocol to the IMA DPU with an interface identical to the corresponding hardware used on the Rosetta mission. All interface lines are buffered *via* special circuits to protect the instrument from external noise effects. The DPU board is controlled by a 24 MHz crystal, which is divided down to 12 MHz and buffered inside the FPGA before it is used for FPGA and processor operations, and on the housekeeping board. The main FPGA requires a 2.5 V operational voltage. This is generated by dedicated regulators directly on the DPU and on the HK board. The watchdog circuit inside the FPGA can be enabled by software. Then the watchdog circuit requires resetting by software access. Otherwise the watchdog circuit issues a hardware reset to the DPU board (after 16 s). Except for a special error message, the reset behavior is identical to a boot sequence initiated after power-up. The DPU board controls most detector voltages with direct access to the HVPS board (NPI, NPD) or the ELS power supply.

3.7.2. *Housekeeping Board (HK)*

A separate RT54SX32S FPGA, which maps all input, controls the HK board and output functions into standard bus address space. It also implements the needed counters for detector pulses from NPI and ELS. Four eight-channel analog multiplexers select one out of 32 analog voltages to be monitored. They are digitalized by one 14-bit ADC LTC1419. Another 14-bit ADC monitors the ELS deflection voltage. Two 8-bit DACs generate control voltages for NPD, NPI, ELS and the scanner *via* 8 latching buffers. The sun sensor electronics is implemented on the HK board.

3.7.3. *Software*

When the instrument is switched on, a boot loader copies the basic program from the bipolar PROM into RAM, switches the PROM off and starts monitoring the TC interface for possible boot instructions. This allows the configuration of the instrument to be flexible, but in a safe manner. If a start configuration is defined *via* TC, the software continues accordingly. Otherwise the default start configuration inside the EEPROM is used. If this is corrupted, the original default configuration from PROM will be used. The software is built around a real-time system with a scheduler and an interrupt handler. All executable routines are defined inside a routing table, which resides in EEPROM and can be modified during flight. In this way, new or modified software routines can be stored inside a free area of the EEPROM, verified and added to the operating software by including their start address into this routing table. A macro feature of the TC handler offers the possibility to generate sequences of standard TC automatically according to a predefined list, reducing the need for complex TC groups to be uplinked over and over again. Besides detector activation and parameter control, compression and averaging of measurement data allow the reduction of the amount of telemetry generated.

3.7.4. *DC/DC Electronics and High Voltage Power Supply (HVPS)*

The ASPERA-3 DC/DC electronics is build around four Interpoint DC/DC converters type HL which provide ± 5 V, ± 12 V, $+5$ V, and -5 V respectively. There are no redundant converters. Because of the extremely tight mass budget it was decided not to have separate switches for the individual sensors (NPI, NPD1, NPD2, ELS). Separate switching is only implemented for IMA (± 5 V, ± 12 V, $+5$ V, and -5 V). All sensors are powered when the instrument is switched on. There are, however, individually controlled 28 V switches for each sensor, which provide power for the sensor high voltage supplies.

The MU HVPS provides high voltages for NPI, NPD1, and NPD2. The general design is similar to the IMA high voltage power supply. A single high voltage supply provides a base voltage, which is regulated by AMPTEK HV601B optocouplers for the sensor use. The regulation accuracy is 256 steps for each range which is sufficient for this application. The base supply uses a common coil transformer followed by a custom-made doubler space qualified in a number of missions.

The NPI HVPS uses two base supplies generating two voltages, namely, an MCP bias in the range from 0 V down to -4300 V and a deflector bias from 0 to $+5000$ V. The fast (1 ms fall/rise time) alternative mode for the deflector voltage is provided by an AMPTEK HV601B optocoupler. Each NPD sensor has an individual HVPS which is built around two base supplies. The single polarity supply provides one base voltage from 0 to 3000 V which is regulated by two AMPTEK optocoules to bias individually START and STOP (all three at one) MCP assemblies. The second double polarity supply provides two voltages from 0 V to $+5000$ V and -5000 V for the NPD double polarity deflector.

3.8. Solar Sensors and MCP Protection

Direct solar light reaching NPI and NPD aperture would cause overload of the MCP based detectors. If the Sun illuminates the sensor only for a short period during scanning, the expected extracted charge over the nominal mission would be around 0.1–0.2 Coulomb/cm^2 for the NPD MCPs and 2 Coulomb/cm^2 for NPI. These levels of the extracted charge are a factor of 100 above those resulting in the MCP gain drop by a factor of 2 in chevron configuration (Malina and Coburn, 1984). Therefore, a system to protect the MCPs was implemented for the ENA sensors. The charged particle sensors, ELS and IMA, are basically immune to the direct solar light. Since the spacecraft attitude and the instrument accommodation were such that the Sun unavoidably reaches the NPI and NPD apertures when the instrument is in the scanning mode, a system to decrease the respective MCP bias voltages on approximately 30% (around 1 kV) for the required period was implemented. The system consists of a high voltage shutter (HVS) which operates when the instrument is in a scanning mode only and includes three different HVS based on different criteria for MCP voltage reduction control. The three HVS are NPD Count HVS, External HVS, and Solar Sensor HVS. Selection of the HVS type is made by a TC. Only one HVS can function at any time.

The NPD Counts HVS is based on continous monitoring of the NPD START count rate (non-correlated). When the count rate exceeds a certain (TC given) threshold, the MCP bias voltages are reduced for a certain (also TC given) period. The disadvantages of this method are a long response time, sensitivity to non-Sun related disturbances, and the difference between the NPI, NPD1, and NPD2 field of view. External HVS reduces the MCP bias voltages over a certain range of scanner positions given by a TC. The required range is defined on the ground from the analysis of the spacecraft altitude. This method was found not to be flexible enough and cannot be used when the spacecraft is in non-Sun related pointing modes, for example, nadir pointing.

The most advanced HVS uses autonomous detection of the Sun position during scanning with two solar sensors. The solar sensors are mounted inside the NPI sensor (Figure 8). Each sensor has $4.2^\circ \times 90^\circ$ field of view (see their apertures in Figure 7) and built around a photodiode sensitive to the solar UV. The bore-sight direction of each sensor makes the 75° angle to the instrument scanning axis. If the Sun is within the solar sensor field of view, the sensor generates a TTL signal. When the Solar Sensor HVS is enabled, the instrument first makes a scan with no HV switched-on and identifies the Sun position. The DPU calculates the respective scanner positions for the NPI, NPD1, and NPD2 sensors where the respective HV must be reduced.

3.9. Ground Support Equipment

Each sensor, ELS, NPI, NPD, and IMA have their individual EGSEs (Electrical Ground Support Equipments). The sensor EGSEs are used during calibrations and verification on the sensor level. The sensor EGSEs are built around Linux PCs with peripheral interface electronics to communicate with the sensors. External standard laboratory voltage supplies are used to power the sensor. The instrument level EGSE emulates the spacecraft OBDH (On Board Data Handling) and power system. It was also built around a Linux PC with the peripheral interface electronics and power system.

The instrument contains contamination sensitive detectors (MCPs) and surfaces (NPD STOP surfaces). To protect the instrument during ground activities, red-tagged covers enclose all sensor apertures and both MU and IMA were constantly purged by nitrogen. The purging inlets were installed directly in the covers, one for IMA, and three for MU (NPD1, NPD2, and ELS/NPI assembly). Purging Ground Support Equipment (PGSE) provided the constant flow (1 l/min) of nitrogen and the distribution between different units.

4. Instrument Accommodation and Operations

ASPERA-3 is externally mounted on the Mars Express bus (Figure 37). The accommodation was chosen (1) to minimize blocking of the instrument field of view by the spacecraft body, (2) to co-aligned the central plane of the IMA field of view with the ecliptic plane when the spacecraft is in the Earth pointing mode, (3) to locate the instrument away from the altitude thruster plumes, (4) to satisfy the bus mechanical requirements. The instrument scanning axis is co-aligned with the +Zb axis (Figure 37). During scanning the +Zb hemisphere is covered.

The main pointings used throughout the mission are the nadir pointing (the Zb axis points toward the local nadir) and the Earth (communication) pointing when −Xb points toward the Earth and Yb is perpendicular to the ecliptic plane. A number of special pointings are also available but most of the time the following profile is applied. The spacecraft is in the Earth pointing throughout the entire orbit except for 40 min around pericenter when it is in the nadir pointing for planetary surface and atmosphere observations. Slews to change from one pointing to another normally take 20–30 min. Therefore, the solar direction (close to the solar wind flux) is always within the IMA field of view when the spacecraft is in the Earth pointing. When the spacecraft is in the Nadir pointing, Mars is within NPI and NPD field of view. For electrons the spacecraft pointing is less critical. The scanner parking position is either the ELS/NPI central axis points in the direction of the −Yb axis, so called 90° position (as shown in Figure 37), or it points in the direction of +Xb, 0° parking position. If the instrument is parked in the 90° position, NPI cannot be operated in the Earth pointing because the Sun is in its field of view.

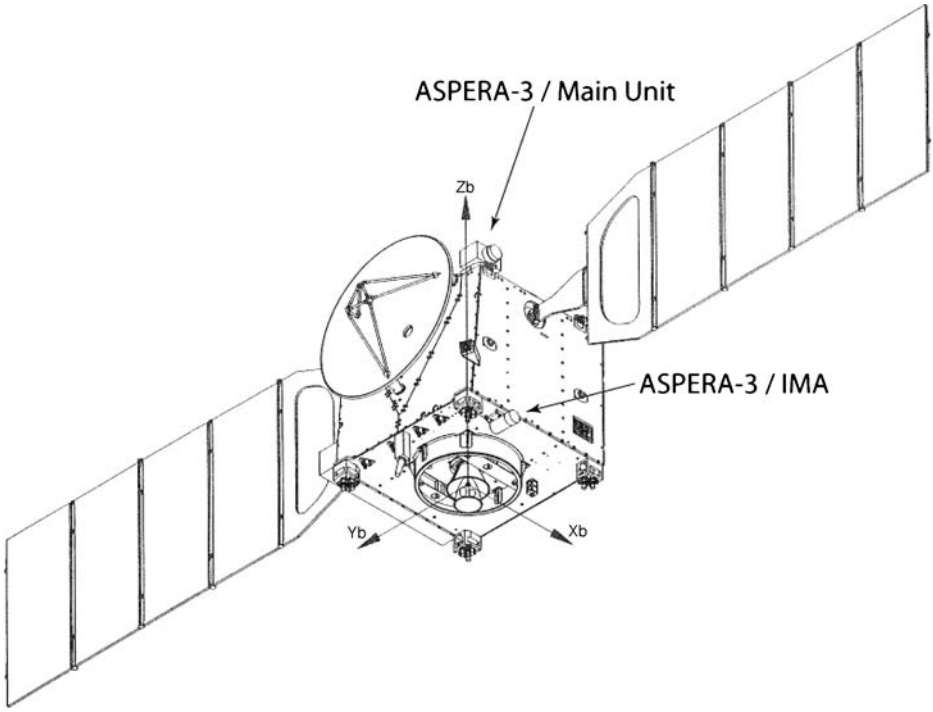

Figure 37. ASPERA-3 accommodation on the Mars Express bus (Courtesy of ASTRIUM, Toulouse).

The typical ASPERA-3 operational profile is as follows. IMA and ELS begin science data taking 20 min prior to the modeled inbound bow shock crossing and stop 20 min after the outbound crossing. ELS is run in the 128 energy step mode (full spectrum per 4 s). IMA is run in the full mode giving 32 masses $\times$16 azimuths $\times$96 energies $\times$16 elevations matrix per 192 s. NPI and NPD are operational during nadir pointing only. NPI provides measurements of the signals from 32 directions with the sampling time 1 s. During different phases of the missions NPD is run in either the binned matrix mode or TOF mode. Because of very high TM demand, the RAW mode is used very seldomly.

5. Summary

The ASPERA-3 experiment is a comprehensive plasma package used to measure ions, electrons, and ENAs. It is for the first time such detailed particle measurements are conducted at Mars. However, because of the absence of field and wave experiments onboard Mars Express, the ASPERA-3 objectives concentrate on the studies of the solar wind impact with the Martian atmosphere. ASPERA-3 is instrumental in defining the current escape rates of the Martian atmosphere, and thus, defining the evolutionary impact of the solar wind interaction.

For the first time, ASPERA-3 performs ENA imaging of a non-magnetized atmospheric body. Due to severe mass constrains, the ENA sensor geometrical factors could not be made large by simply increasing the size of the instrument. Therefore, an entirely new technique, ENA surface reflection, was developed and implemented. The ENA results reported in this issue as well as previous publications (see references in this issue ENA papers) clearly indicate that the technique works.

A replica of the ASPERA-3 experiment, ASPERA-4, is currently operational on an orbit at Venus onboard the Venus Express mission launch 2003. This makes the ASPERA-3 experiment a unique tool to be used in comparative magnetospheric studies.

Appendix. List of Acronyms

ADC	Analog-To-Digit Converter
ASPERA	Analyzer Of Space Plasmas And Energetic Atoms
DAC	Digit-To-Analog Converter
DigTOF	Digital TOF Electronics
DPU	Digital Processing Unit
EEPROM	Electrically Erasable Programmable Read Only Memory
EGSE	Electrical Ground Support Equipment
ELS	Electron Spectrometer
ENA	Energetic Neutral Atoms
ESA	Electrostatic Analyzer
FEE	Front End Electronics
FPGA	Field Programmable Gate Array
FWHM	Full Width At Half Maximum
HK	House Keeping
HVS	High Voltage Shutter
HVPS	High Voltage Power Supply
ICA	Ion Composition Analyzer
IMA	Ion Mass Analyzer
IMAGE	Imager For Magnetopause-To-Aurora Global Exploration
IMI	Ion Mass Imager
IMIS	Iona Mass Imaging Sensor
LENA	Low Energy Neutral Atoms
MAG/ER	Magnetometer And Electron Reflectrometer
MCP	Microchannel Plate
MEDUSA	Miniaturized Electrostatic Dual-Top-Hat Spherical Analyzer
MGS	Mars Global Surveyor

MOCAD	Monolitic Octal Charge Amplifier/Pulse Discriminator
MU	Main Unit
NPI	Neutral Particle Imager
NPD	Neutral Particle Detector
OBDH	On Board Data Handling
RAM	Random Access Memory
PGSE	Purging Ground Support Equipment
PHD	Pulse Height Distribution
PIPPI	Prelude In Planetary Particle Imaging
PROM	Programmable Read Only Memory
SE	Secondary Electrons
SRAM	Static RAM
TC	Telecommand
TDC	Time-To-Digit Converter
TICS	Three-Dimensional Ion Composition Spectrometer
TM	Telemetry
TMU	TDC Management Unit
TOF	Time-Of-Flight
TTL	Transistor-Transistor Logic

Acknowledgements

The ASPERA-3 experiment on the European Space Agency Mars Express mission is a joint effort between 15 laboratories in 10 countries, all sponsored by their national agencies as well as the various departments/institutes hosting these efforts. We also wish to acknowledge the Swedish National Space Board for their support of the main Principle Investigator institute, Swedish Institute of Space Physics, Kiruna, and we are indebted to European Space Agency for its courage in embarking on the Mars Express program, the first European mission to the red planet. We acknowledge contributions from Imperial college, London, UK for providing the IEEE-1335 link chips used in the IMA sensor and NASA NASW-0003 for providing the ELS sensor.

References

Acuña, M. H., *et al*.: 1998, *Science* **279**, 1676.

Alsop, C., Free, L., and Scott, S.: 1996, UV rejection design and performance of the Cluster PEACE 'top-hat' electrostatic analyser, submitted to *Proc. AGU Chapman Conference on Measurement Techniques in Space Plasmas*.

Barabash, S.: 1995, *IRF Scientific Report* **228**.
Barabash, S., Fedorov, A., Lundin, R., and Sauvaud, J.-A.: 2007, *Science* (in press).
Barabash, S., Holmström, M., Lukyanov, A., and Kallio, E.: 2002, *J. Geophys. Res.* **107**(A10), 1280, doi:10.1029/2001JA000326.
Bertaux, J.-L., Leblanc, F., Witasse, O., Quemerais, E., Lilensten, J., Stern, S. A., *et al.*: 2005, *Nature* **435**, doi:10.1038/nature03603.
Bibring, J.-P., Langevin, Y., Gendrin, A., Gondet, B., Poulet, F., Berth, M., *et al*: 2005, *Science* **307**, 1576.
Brecht, S. H.: 1997, *J. Geophys. Res.* **102**, 11287.
Brinkfeldt, Klas, Instrumentation for Energteic Neutral Atom Measurements at Mars, Venus, and the Earth: 2005, *IRF Scientific Report 288*, Ph.D. thesis.
Brinkfeldt, K., Gunell, H., Brandt, P., Barabash, S., Frahm, R. A., Winningham, J. D., *et al.*: 2006, *Icarus* **182**, 439.
C:son Brandt, P., Barabash, S., Wilson, G. R., Roelof, E. C., and Chase, C. J.: 2000, *J. Atmos. Solar Terrestrial Phys.* **62**, 901.
Carlsson, E., Fedorov, A., Barabash, S., Budnik, E., Grigoriev, A., Gunell, H., *et al.*: 2006, *Icarus* **182**, 320.
Collier, M. R., Moore, T. E., Ogilvie, K. W., Chornay, D., Keller, J. W., Boardsen, S., *et al.*: 2001, *J. Geophys. Res.* **106**, 24893.
Crider, D., Acuña, M., Connerney, J., Vignes, D., Ness, N., Krymskii, A., *et al.*: 2002, *Geophys. Res. Lett.* **29**(8), 1170.
Early, D. S., and Long, D. G.: 2001, *IEEE Trans. Geosci. Remote Sensing* **39**, 291.
Fox, J. L.: 1997, *Geophys. Res. Lett.* **24**, 2901.
Futaana, Y., Barabasha, S., Grigoriev, A., Winningham, D., Frahm, R., and Lundin, R.: *Space Sci. Rev.*, this issue, doi: 10.1007/s11214-006-9026-9.
Galli, A., Wurz, P., Barabash, S., Grigoriev, A., Gunell, H., Lundin, R., *et al.*: *Space Sci. Rev.*, this issue, doi: 10.1007/s11214-006-9088-8.
Grigoriev, A., Futaana, Y., Barabash, S., and Fedorov, A.: *Space Sci. Rev.*, this issue, doi: 10.1007/s11214-006-9121-y.
Gunell, H., Holmström, M., Barabash, S., Kallio, E., Janhunen, P., Nagy, A. F., *et al.*: 2006, *Plane. Space Sci.* **54**, 117.
Holmström, M., Barabash, S., and Kallio, E.: 2002, *J. Geophys. Res.* **107**(A10), 1277, JA000325.
Jans, S.: 2000, Ionization of energetic neutral atoms for application in space instrumentation, Diplomarbeit der Philosophisch-naturwissenschaftlichen Fakultät det Univerität Bern.
Johnstone, A. D., Alsop, C., Burge, S., Carter, P. J., Coates, A. J., Coker, A. J., *et al.*: 1997, in C. P. Escoubet, C. T. Russell, and R. Schmidt (eds.), Kluwer Academic: Dordrecht, Netherlands, *Space Sci. Revs.* **79**, 351.
Kallio, E.: 1996, *J. Geophys. Res.* **101**, 111333.
Kallio, E., Luhmann, J. G., and Barabash, S.: 1997, *J. Geophys. Res.* **102**, 22183.
Kallio, E., and Janhunen, P.: 2001, *J. Geophys. Res.* **106**, 5617.
Kallio, E., and Barabash, S.: 2000, *J. Geophys. Res.* **105**, 24973.
Kallio, E., and Barabash, S.: 2001, *J. Geophys. Res.* **106**, 165.
Kallio, E., Barabash, S., Brinkfeldt, K., Gunell, H., Holmström, M., Futaana, Y., *et al.*: 2006, *Icarus* **182**, 448.
Krymskii, A. M., Breus, T. K., *et al.*: 2003, *J. Geophys. Res.* **108**(A12), 1431.
Lammer, H., Lichtenegger, H. I. M., Kolb, C., Ribas, I., Guinan, E. F., Abart, R., *et al.*: 2003, *Icarus* **165**, 9.
Lichtenegger, H., Lammer, H., and Stumptner, W.: 2002, *J. Geophys. Res.* **107**(A10), 1279, doi: 10.1029/2001JA000322.
Luhmann, J. G., and Kozyra, J. U.: 1991, *J. Geophys. Res.* **96**, 5457.

Luhmann, J. G., *et al.*: 1992, *Geophys. Res. Lett.* **19**, 2151.
Lundin, R., *et al.*: 1991, *Geophys. Res. Lett.* **18**, 1059.
Lundin, R., Barabash, H., Andersson, M., Holmström, A., Grigoriev, M., Yamauchi, J.-A., *et al.*: 2004, *Science* **305**, 1933.
Lundin, R., Winninghan, D., Barabash, S., Frahm, R., Holmström, M., Sauvaud, J.-A., *et al.*: 2006, *Science* **311**(5763), 980.
Malina, R. F., and Coburn, K. R.: 1984, *IEEE Trans. Nuclear Sci.* **NS-31**, 404.
Marshall, F. J., Hardy, D. A., Huber, A., Pantazis, J., McGarity, J., Holeman, E., *et al.*: 1986, *Rev. Sci. Instrum.* **57**(2), 229.
Mura, A., Milillo, A., and Orsini, S.: 2002, *J. Geophys. Res.* **107**(A10), 1278, doi: 10.1029/2001JA 000328.
Nilsson, H., Carlsson, E., Gunell, H., Futaana, Y., Barabash, S., Lundin, R., *et al.*: *Space Sci. Rev.*, this issue, doi: 10.1007/s11214-006-9030-0.
Nairn, C. M. C., Grard, R., Skalsky, A., and Trotignon, J. G.: 1991, *J. Geophys. Res.* **96**, 11227.
Norberg, O., Yamauchi, M., Lundin, R., Olsen, S., Borg, H., Barabash, S., *et al.*: 1998, *Earth, Planets, Space* **50**, 199.
Norberg, O., Winningham, J. D., Lauche, H., Keith, W., Puccio, W., Olsen, J., *et al.*: 2001, *Ann. Geophys.* **19**, 593.
Roelof, E. C., and Skinner, A. J.: 2000, *Space Sci. Rev.* **91**, 437.
Sablik, M. J., Scherrer, J. R., Winningham, J. D., Frahm, R. A., and Schrader, T.: 1990, *IEEE Trans. Geosci. Remote Sensing* **28**, 1034.
Terada, N., Machida, S., and Shinagawa, H.: 2002, *J. Geophys. Res.* **107**, doi:10.1029/2001JA009224.
Verigin, M., *et al.*: 1991, *J. Geophys. Res.* **96**, 19315.